eROSITA All-Sky Survey 1: Study of the Canis Major Dwarf Spheroidal Galaxy

Bachelorarbeit aus der Physik

Vorgelegt von

Theresa Heindl

12. April 2021

Dr. Karl Remeis-Sternwarte
Friedrich-Alexander-Universität Erlangen-Nürnberg

Betreuerin: Prof. Dr. Manami Sasaki

Abstract

This work is a population study of the Canis Major Dwarf Spheroidal Galaxy which is believed to be a dwarf satellite galaxy to the Milky Way. It is located close to the galactic plane at (l, b) = (240°, -8°). The aim of this thesis was to identify possible Canis Major sources in eROSITA data. X-ray data of the eROSITA All-Sky Survey 1 was studied and analysed by looking at the X-ray properties of the 17 676 detected sources and by calculating hardness ratios and the X-ray-to-optical flux ratio. This analysis resulted in the conclusion that the eROSITA standard bands are not useful for hardness-ratio based analysis and need to be adjusted for better comparability.

The observed X-ray sources were cross-matched with four other multiwavelength catalogues in order to determine the class of sources: the optical Gaia and Skymapper catalogues, and the (near) infrared 2MASS and WISE catalogues. Through criteria by Wright et al. (2010), background object candidates, foreground star and elliptical galaxy candidates as well as normal galaxy candidates were identified with WISE data. By analysing colour-magnitude diagrams of Gaia matches and theoretical isochrones, more galactic foreground and distant background candidates were excluded. A criterion based on the work of Martin et al. (2004) identified a selection of Canis Major candidates on the red giant branch in 2MASS magnitudes. Hardness ratio models suggest that most candidates have thermal emission with low temperature and low absorption. Applying all criteria, 1289 final Canis Major candidates were identified and should be further discussed in future studies.

Contents

List of Tables

List of Figures

1 Introduction

Throughout the Universe, galaxies are never found as stand-alone objects but always in a minimum of pairs or clusters. They are not evenly distributed in space but rather can be found in groups. Due to this characteristic, the evolution of galaxies does not happen in isolation. Each galaxy interacts with several others of their cohort through collisions or encounters during their lifetime. In the case of smaller galaxies interacting with bigger ones, it is possible that tidal forces rip the smaller one apart and merge it with the bigger one (Karttunen et al., 2017).

Regarding our Milky Way galaxy, 27 galaxies are associated with its subgroup (McConnachie, 2012). Two well known satellite galaxies of the Milky Way are the Large and Small Magellanic Clouds which are at a distance of about 60 kpc. Computations suggest that those two satellites will merge with the Milky Way during their next close approach (Karttunen et al., 2017). The closest known satellite galaxy of the Milky Way is the Canis Major dwarf galaxy at a distance of 8 kpc (Martinez-Delgado et al., 2005).
The Canis Major dwarf Spheroidal Galaxy is an elliptical stellar overdensity in the Canis Major constellation located at $(l, b) = (240°, -8°)$ and was first identified by Martin et al. (2004). It is positioned close to the Galactic plane and believed to be in the process of being pulled apart by gravitational forces of the Milky Way galaxy. Its distance from the galactic centre is $d_{GC} = 12.0$ kpc ± 1.2 kpc. There was a M-giant overdensity detected which is similar in number to that in the core of the Sagittarius dwarf galaxy. Because of that, it is assumed that the Canis Major overdensity is an old dwarf satellite galaxy which is accreted onto the Milky Way plane (Martin et al., 2004).

This work will pursue the findings of previous discoveries which are mostly based on infrared observations to find more information about the population of the Canis Major dwarf galaxy through X-ray observations.

2 Background Information

To gain a better understanding of the conducted research, this chapter conveys the fundamental information about stellar evolution, X-ray sources and the eROSITA mission.

2.1 Stellar Evolution

Stellar evolution begins in a gas cloud with the formation of a protostar. Depending on the accreted mass, either a planet, brown dwarf or main sequence star is born. Lifespans of main sequence stars range from 10^7 to 10^{11} years depending on their mass. Lower mass stars have a longer life span, more massive ones a shorter one which also influences their path of life (Karttunen et al., 2017).

A Hertzsprung-Russell Diagram (HRD) as seen in Fig. 2.1 shows the luminosity of stars as a function of effective temperature and thereby gives information about their properties, masses, age and current stage in stellar evolution. The central diagonal branch is called main sequence and consists of stars that fuse hydrogen into helium. When their hydrogen supply is exhausted, they turn off the main sequence and turn into supergiants, giants or white dwarfs according to their initial masses (ESO, 2007).

A low mass star starts on the main sequence with hydrogen core burning. This phase is the longest and most stable stage in the life of a star and can be seen in the HRD in Fig. 2.1 as a diagonal branch spanning across the diagram. After all centre hydrogen is burned up, its main sequence phase comes to an end and the star moves horizontally to the right in the HRD to the subgiant branch with hydrogen shell burning. As the hydrogen shell burning increases its helium mass and luminosity, the now so-called red giant moves upwards in the HRD. At the end of this branch, there are several options. Stars which suffered from too much mass loss will evolve directly into white dwarfs. If the stars' mass is less than than 2.3 $M_\odot$, the helium ignites and causes a flash in the core. This energy release increases the temperature and expands the core of the star, moving it to the horizontal branch. After the helium in the core is exhausted, the star reaches the asymptotic giant branch, where burning of heavier elements can be realised. As

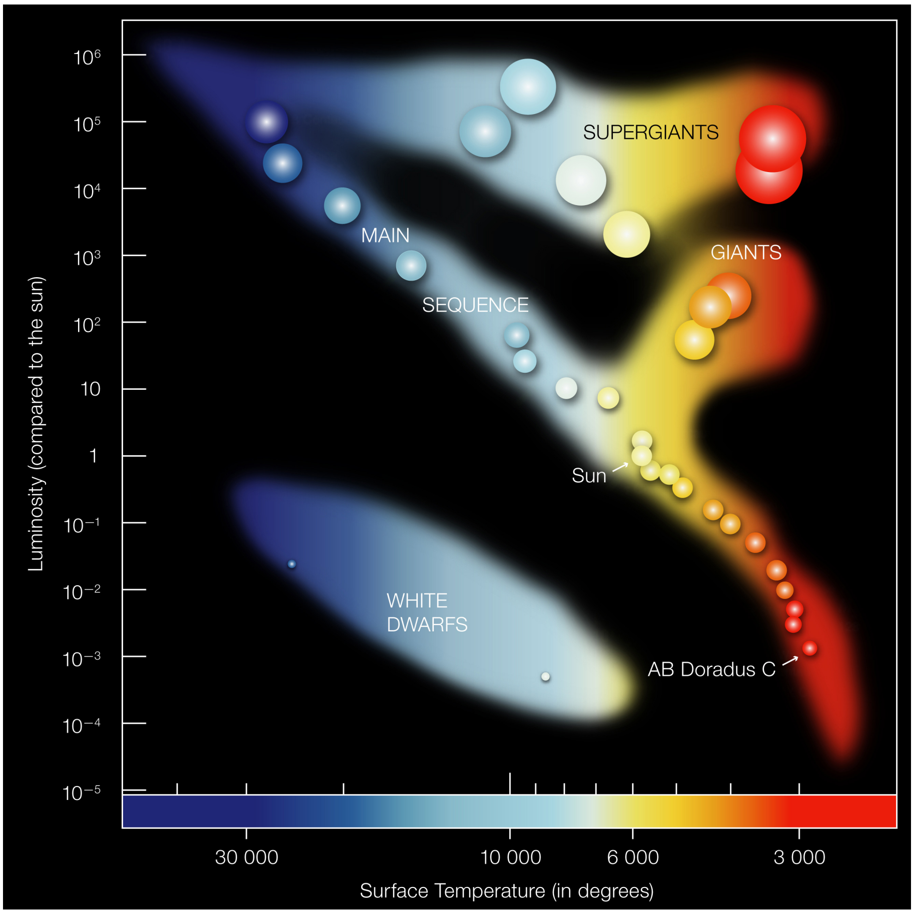

Fig. 2.1: Hertzsprung-Russell Diagram showing the temperatures of stars against their luminosities. Credit: ESO (2007)

soon as no more stages of burning can be ignited, its outer layers will be ejected and become a planetary nebula with the remnant of the star being a white dwarf. The white dwarf group can be found in the bottom left of the HRD.
Massive stars on the other end have a different fate. If their initial mass is bigger than 8 $M_\odot$, the temperature in the core can reach higher temperatures thus being able to do more extensive shell and core burning up to iron. When no more energy is produced, there is also no gravity-counteracting pressure left and the core collapses resulting in a supernova. Depending on the remaining mass, either a black hole or a neutron star is formed (Karttunen et al., 2017).

2.2 eROSITA Mission and X-Ray Sources

The extended ROentgen Survey with an Imaging Telescope Array (eROSITA) was launched on the Russian Spektrum-Roentgen-Gamma (SRG) mission on July 13, 2019. The programme aims to perform eight all-sky surveys to provide the to date most sensitive observations in soft X-rays (0.2–2.3 keV), and the first ever image in hard X-rays (2.3–8 keV). This survey is called the eROSITA All-Sky Survey (eRASS) and there will be eight surveys in total until 2023, each lasting half a year (Predehl et al., 2021).

Fig. 2.2 shows the schematics of the eROSITA X-ray telescope. The core of the telescope consists of seven identical mirror arrays with a charge-coupled-device (CCD) camera in each focus point. Each CCD has 384x384 pixels with an image area of 28.8 mm x 28.8 mm, the optimal operation temperature is at -85°C. In order to protect the CCDs from cosmic particles, shields of copper and aluminium are used. The mirrors are of the type Wolter-I, each a combination of 54 paraboloid and hyperboloid mirrors which are especially used for X-ray telescopes. To counteract the detection of photons from beyond the field of view, X-ray baffles are placed in front of the mirror module (Predehl et al., 2021).

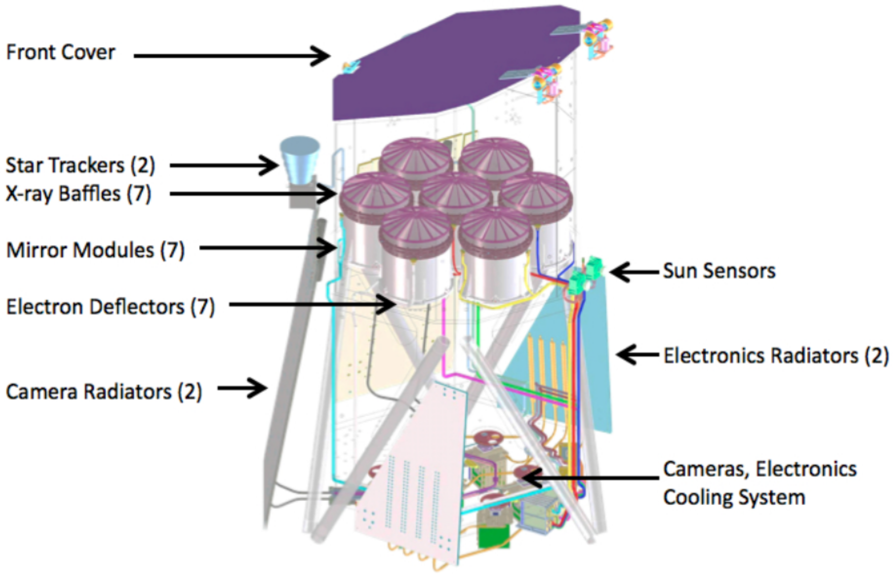

Fig. 2.2: Schematic of the eROSITA telescope. Labels show the name and quantity of the parts. Taken from Merloni et al. (2012).

The goal of the mission is to study the most massive structures and galaxy clusters in the universe up to redshifts of $z > 1$ to test cosmological models including Dark Energy, and to gain an improved set of X-ray data. The soft X-ray band (0.2–2.3 keV) will be 25 times more sensitive than the ROSAT All-Sky Survey and in the X-ray hard band (2.3–8 keV), the first ever true imaging survey of the sky will be completed with eROSITA. The extent of the energy band range compared to other X-ray surveys can be found in Fig. 2.3 (Predehl et al., 2021).

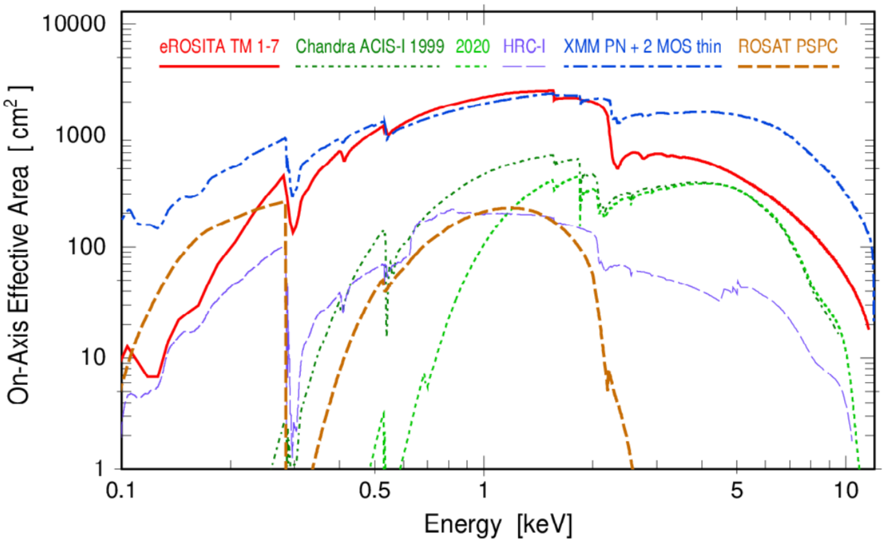

Fig. 2.3: On–axis effective areas per energy band. eROSITA (red), Chandra ACIS-I (green), Chandra HRC-I (purple), XMM-Newton (blue), and ROSAT (brown) bands are plotted for comparison (Predehl et al., 2021).

New insights into other astrophysical phenomena linked with X-ray sources like X-ray binaries, active stars, and diffuse emission within the Galaxy are expected as well as the study of a few million active galactic nuclei (AGNs) to revolutionise the view of supermassive black holes.

The first all-sky survey started on December 13, 2019. The resulting first image of eROSITA can be found in Fig. 2.4 and shows some of the previously mentioned X-ray phenomena very clearly. About one million X-ray sources have been detected in this image. The whole sky is shown as Aitoff projection where the centre of the Milky Way is in the middle. The detected photons have been colour-coded according to their energy bands, with red representing 0.3 - 0.6 keV, green for 0.6 - 1 keV and blue for 1 - 2.3 keV. The red diffuse glow is emission of hot gas from the Local Bubble, the blue emission in the galactic plane shows high-energy sources as low-energy emission is absorbed by dust and gas. Green and yellow colours represent very hot gas which was rejected out of the galactic centre by supernovae or the now dormant supermassive black hole in the centre of our galaxy among other phenomena. This gas forms two huge bright bubbles in the halo above and underneath the centre of the Milky Way. The southern part was firstly discovered through eRASS1 and is together with the well-known northern bubble also known as eROSITA bubbles. At the right edge of the blue galactic disc, the Vela supernova remnant can be seen in bright yellow. A lot of white X-ray point sources like distant active galactic nuclei can be found uniformly distributed over the sky, while galaxy clusters appear as extended X-ray nebulosities (MPE, 2020a,b).

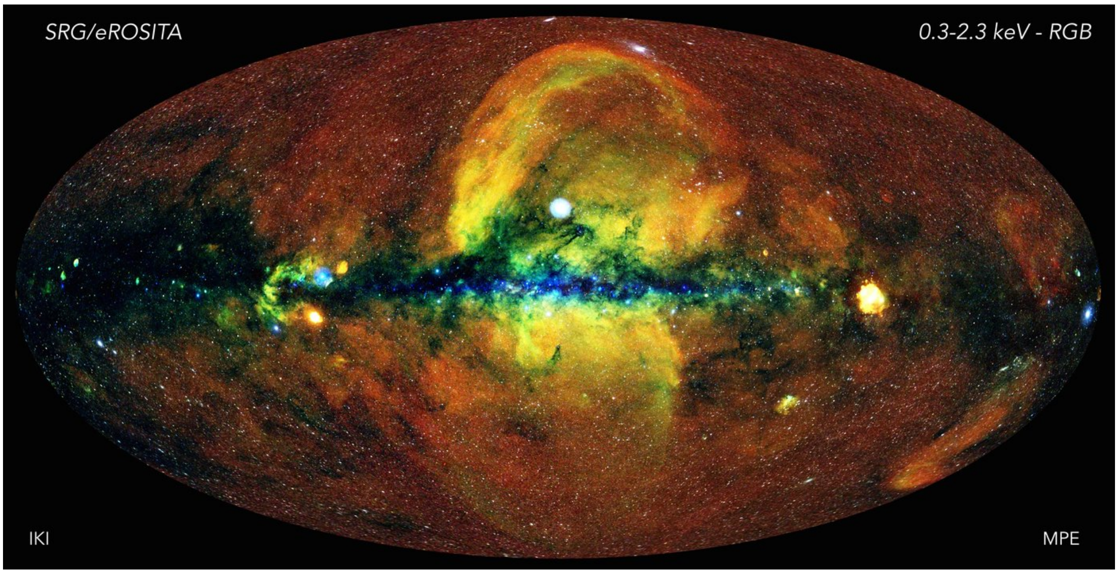

Fig. 2.4: X-ray image of the first eROSITA all-sky survey. Photons have been colour-coded according to their energy (red for 0.3 - 0.6 keV, green for 0.6 - 1 keV, blue for 1 - 2.3 keV). Credit: Jeremy Sanders, Hermann Brunner and the eSASS team (MPE); Eugene Churazov, Marat Gilfanov (on behalf of IKI)(MPE, 2020b).

3 Data Analysis

This chapter uses the data of the eROSITA all-sky survey 1 taken between 13 December 2019 and 11 June 2020 to analyse the region of the Canis Major dwarf spheroidal galaxy.

3.1 eROSITA Catalogue

Two extraction regions as defined in Tab. 3.1 were selected according to Martin et al. (2004) to cover the whole area of the Canis Major dwarf galaxy. The selected region of the sky can be seen as yellow circles in a DSS survey image in Fig. 3.1.

RA[J2000]	DEC[J2000]	Radius (degree)
102.90207	-20.503367	13.2
111.2569	-34.829789	13.2

Tab. 3.1: Coordinates of the circular extraction regions of the Canis Major galaxy based on Martin et al. (2004).

The eRASS1 catalogue was downloaded by Manami Sasaki from the eROSITA data server. Afterwards, exclusively the sources which lie in the extraction region of Tab. 3.1 were chosen via a script written by Manami Sasaki. There were 17 676 sources detected in the selected regions.

3.1.1 Catalogue Contents

The data from the eRASS1 catalogue includes the coordinates and observation IDs of the sources. Furthermore, it provides even more information, including the total number of X-ray counts per energy band $i = 0, 1, 2, 3$ as well as the corresponding errors. The energy band widths of eROSITA can be found in Tab. 3.2. It also contains the count rate for all energy bands which provides the number of counts during a certain exposure time. In the following analysis, the total count rate of $i = 0$ is referred to as $RATE$.

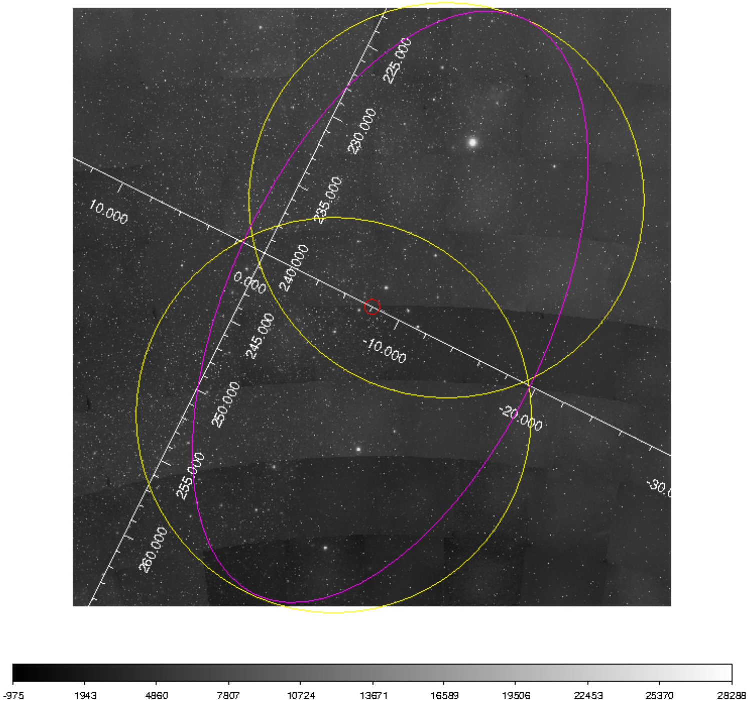

Fig. 3.1: Selected regions of the Canis Major dwarf galaxy visualised by Sara Saeedi in a DSS survey optical image. The two yellow circles mark the two chosen extraction regions based on Tab. 3.1.

Band number i	Energy Range [keV]
0	0.2-5.0
1	0.2-0.6
2	0.6-2.3
3	2.3-5.0

Tab. 3.2: Energy bands of eROSITA.

3.1.2 X-Ray Hardness Ratios

Hardness ratios (HR) are useful to compare the intensity of sources in different energy bands. They were calculated for the eROSITA X-ray data by using equations 3.1 and 3.2 in accordance with Saeedi et al. (2016). Instead of the count rates, the number of counts B_i in each eROSITA band was used because this value is more reliable as it shows the distribution of the total number of counts throughout the energy bands. B_i is the softer band, B_{i+1} the harder band, and EB_i is the corresponding error of the counts. As there are three different energy bands in eROSITA, two hardness ratios

$$HR_i = \frac{B_{i+1} - B_i}{B_{i+1} + B_i} \tag{3.1}$$

and their corresponding errors

$$EHR_i = 2 \cdot \sqrt{\frac{(B_{i+1} \cdot EB_i)^2 + (B_i \cdot EB_{i+1})^2}{(B_{i+1} + B_i)^2}} \tag{3.2}$$

as seen in Saeedi et al. (2016) could be calculated which will be discussed later on in section 3.2.1.

3.2 Multiwavelength Catalogues

The detected eROSITA X-ray sources were cross-matched with the optical Gaia Data release 2 (Gaia Collaboration et al., 2016, 2018), the optical Skymapper (SM) Data Release 1.1 (Wolf et al., 2018), The Wide-field Infrared Survey Explorer (WISE) catalogue (Cutri et al., 2014), and The Two Micron All Sky Survey (2MASS) near-infrared catalogue (Skrutskie et al., 2006) via a version of the NWAY algorithm by Salvato et al. (2017) that was written by Jonathan Knies (Dr. Karl Remeis-Observatory Bamberg).

The counterparts received by this provide important additional information about the objects as an X-ray source may also have emission in other wavelengths. This is the key feature of a population study as without this analysis, identification of different types of objects would be difficult.

From the Gaia catalogue, Gaia's white-light G-band (330–1050 nm), the blue (BP) and red (RP) prismphotometers bands G_{BP}(330–680 nm) and G_{RP} (630–1050 nm) were used as well as the estimated distance of sources. The Skymapper catalogue provided data in its g (centre wavelength at 510 nm) and r (centre wavelength at 617 nm) bands, the WISE catalogue in W1 (3,4 µm), W2 (4,6 µm) and W3 (12 µm) bands. 2MASS data was obtained in J (1,25 µm) and K_s (in the following called K with 2,16 µm) bands. A visualization of the different passbands can be found in Fig. 3.2. The analysis of the various diagrams made with this data will be discussed in the following sections.

X-ray sources which didn't have counterparts in certain catalogues were also plotted for completeness and can be found in the Appendix.

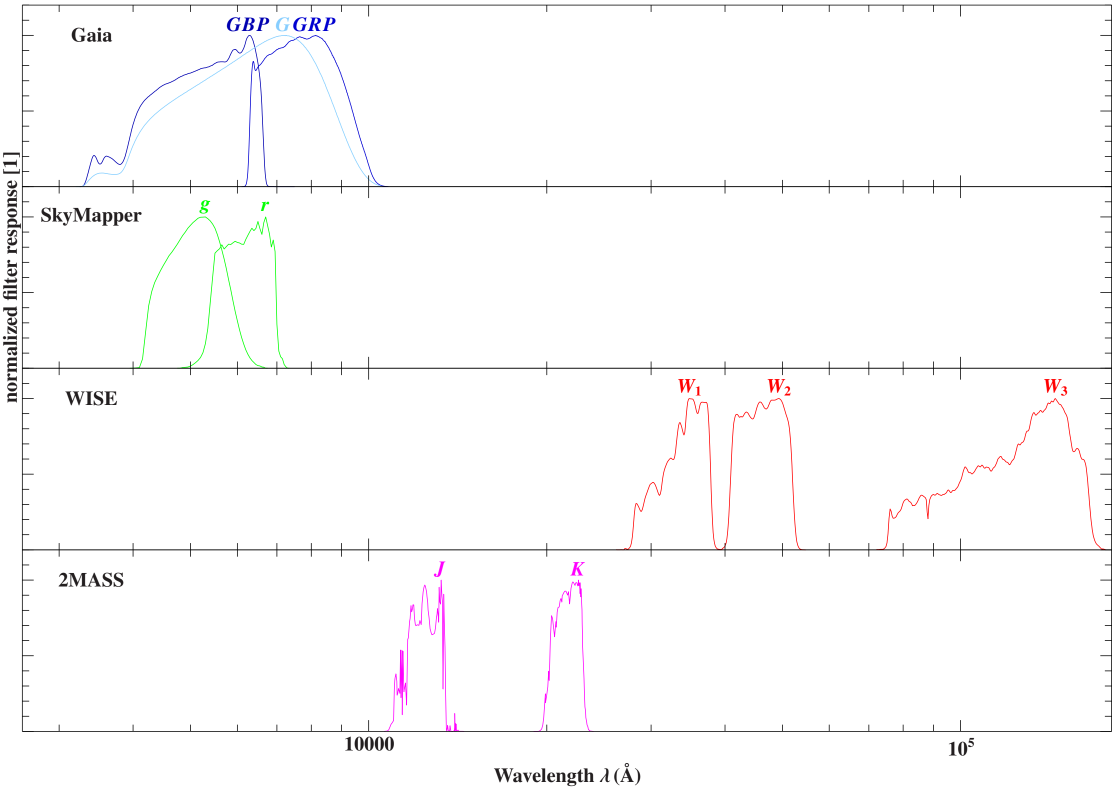

Fig. 3.2: Passbands of the Gaia, Skymapper, WISE and 2MASS surveys as function of wavelength. Created by Steven Hämmerich.

3.2.1 WISE Classification

The first step in identifying possible Canis Major sources was plotting the WISE counterparts in a colour-magnitude diagram as seen in Fig. 3.4 and dividing them in four different classes of sources based on Wright et al. (2010) (see Fig. 3.3 and Tab. 3.3). The four classification types are Galactic Foreground Sources and Elliptical Galaxies (FE), Starburst Galaxies (SB), Active Galactic Nuclei (AGN), and Normal Galaxies (NG). FE sources were marked in blue as they are very likely to consist of stellar and therefore foreground sources. AGN and SB matches were coloured in red for being potential background source. The remaining NG sources were marked in black. Objects from the Canis Major dwarf galaxy can be expected in the FE and NG classes as the galaxy is very close to the galactic plane and a non-active elliptical normal galaxy.

This selection was highlighted in the magnitude diagrams of the counterparts of the remaining catalogues.

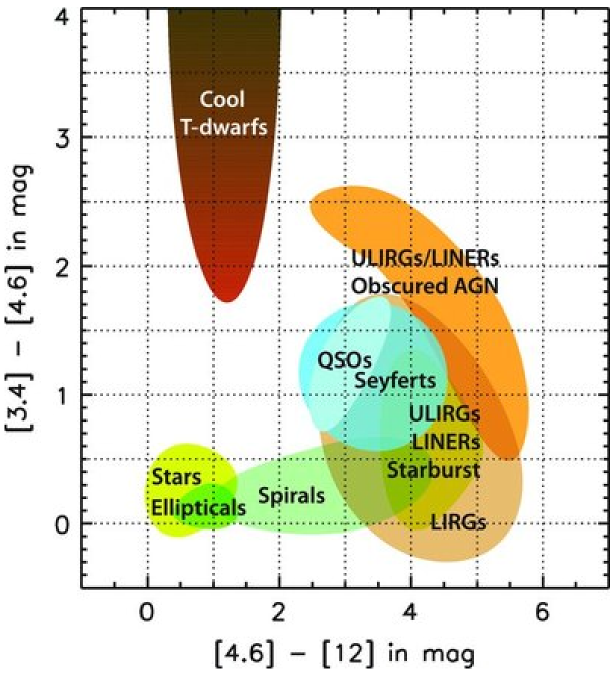

Fig. 3.3: WISE colour-colour diagram of different types of objects. W1 minus W2 band plotted over W2 minus W3 band where the bands are represented in their respective wavelength (Wright et al., 2010).

Type	W2-W3 [mag]	W1-W2 [mag]
FE	≤ 1.5	≤ 0.7
SB	≥ 4.6	≤ 0.7
AGN		> 0.7
NG	$1.5 <$ W2-W3 < 4.6	≤ 0.7

Tab. 3.3: Adjusted critical values of the WISE classification based on Fig. 3.3 by Wright et al. (2010). The four classification types are Galactic Foreground Sources and Elliptical Galaxies (FE), Starburst Galaxies (SB), Active Galactic Nuclei (AGN), and Normal Galaxies (NG).

In the Skymapper magnitude diagram in Fig. 3.5, a separation between blue foreground candidates and red background candidates becomes visible.

The 2MASS magnitude diagram in Fig. 3.6 also shows a separation between blue foreground candidates and black normal galaxy candidates.

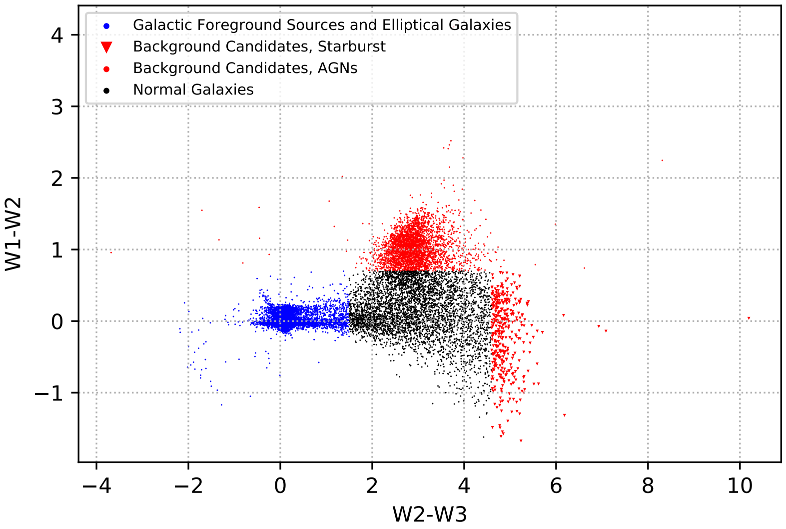

Fig. 3.4: WISE magnitude diagram split in four different candidate types according to the Wright et al. (2010) criteria in Tab. 3.3 and Fig. 3.3.

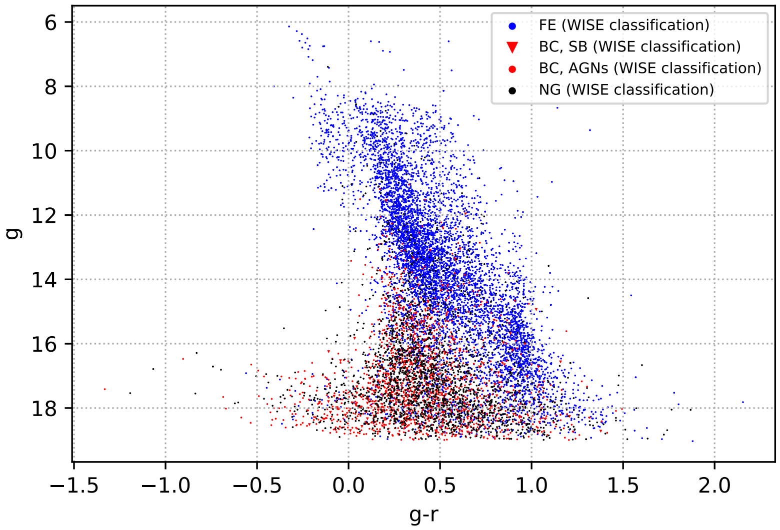

Fig. 3.5: Skymapper magnitude diagram with highlighted classes of objects according to the Wright et al. (2010) criteria in Tab. 3.3 and Fig. 3.4.

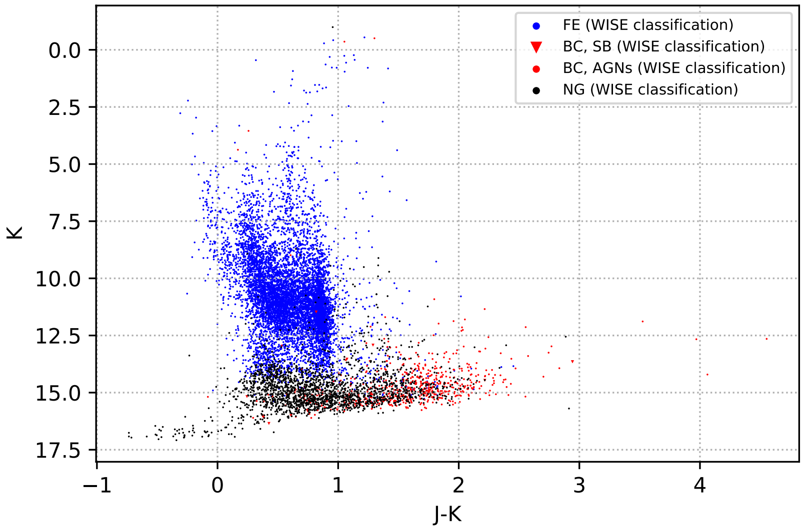

Fig. 3.6: 2MASS magnitude diagram with highlighted classes of objects according to the Wright et al. (2010) criteria in Tab. 3.3 and Fig. 3.4.

Fig. 3.7 shows the comparison of the Skymapper g magnitude to the eROSITA X-Ray countrate. The blue foreground candidates also appear to be separated from the rest.

Furthermore, the hardness ratios calculated in section 3.1.2 are plotted in Fig. 3.8. The sources are again coloured according to the WISE classification (see 3.3). The diagram also shows various models of expected hardness ratio which were created by Sara Saeedi via a PyXspec spectral analysis. Three power-law spectra ($\Gamma =$ 1,2,3) and three black-body spectra (APEC at temperatures of kT= 0.2, 1.0 and 2.0 keV) models were chosen with different column densities (N_H= $0.01 \cdot 10^{22}$ cm^{-2} to $100 \cdot 10^{22}$ cm^{-2}) for correlation. The models only shown a small concordance with the distribution of the sources. A cluster of sources lies in the bottom right of Fig. 3.8 close to the dark green APEC model which suggests thermal emission at low temperatures and low absorption. Moreover, the different types of sources appear to be mixed and no clear separation is possible. This concludes that the standard bands of eROSITA are not useful for further hardness ratio-based analysis.

Next, the calculated hardness ratios were compared to the total X-ray count rate as seen in Fig. 3.9 and Fig. 3.10. Nearly all sources are soft X-ray sources as their HR1 is mostly positive in Fig. 3.9 and HR2 mostly negative in Fig. 3.10.

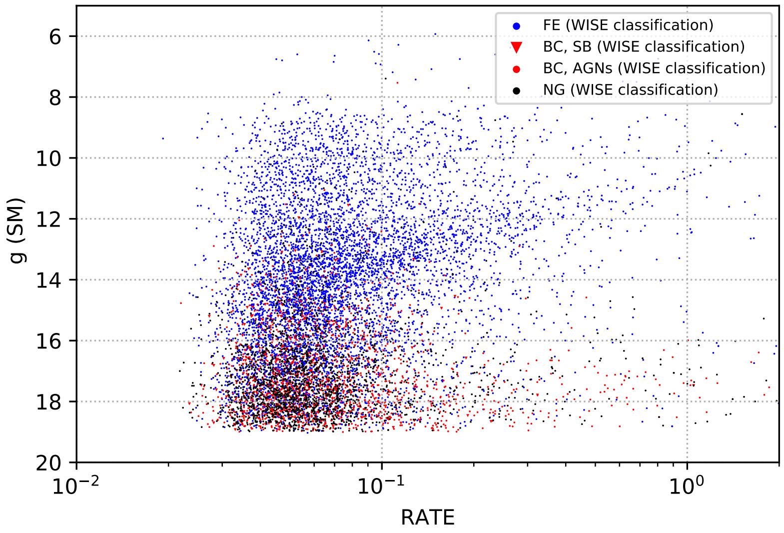

Fig. 3.7: Skymapper magnitudes in relation to the eROSITA X-Ray count rate. The sources are highlighted according to the Wright et al. (2010) criteria in Tab. 3.3 and Fig. 3.4.

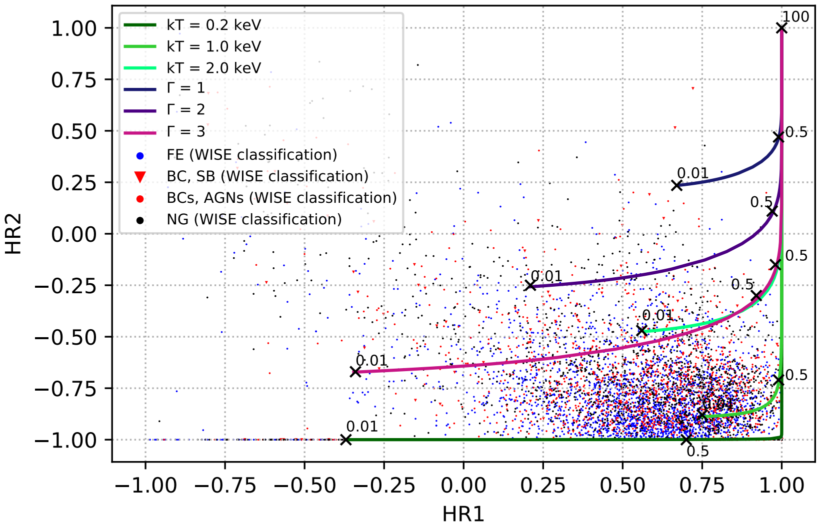

Fig. 3.8: HR diagram with power-law (Γ) and black-body (kT) spectra models. Sources are highlighted according to the Wright et al. (2010) criteria in Tab. 3.3 and Fig. 3.4. Column densities (N_H) are marked by crosses and value in 10^{22} cm^{-2}. Median error on HR1 is 0.26 and 0.23 on HR2.

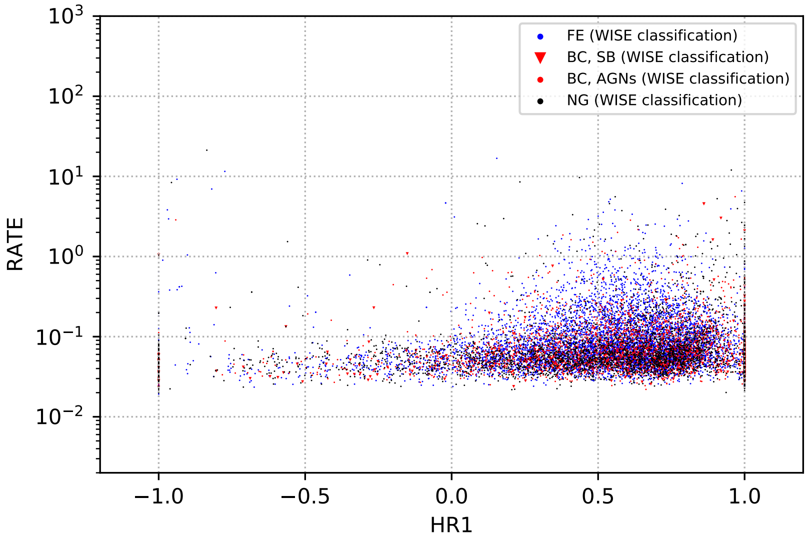

Fig. 3.9: X-ray count rate over hardness ratio 1. The sources are highlighted according to the Wright et al. (2010) criteria in Tab. 3.3 and Fig. 3.4.

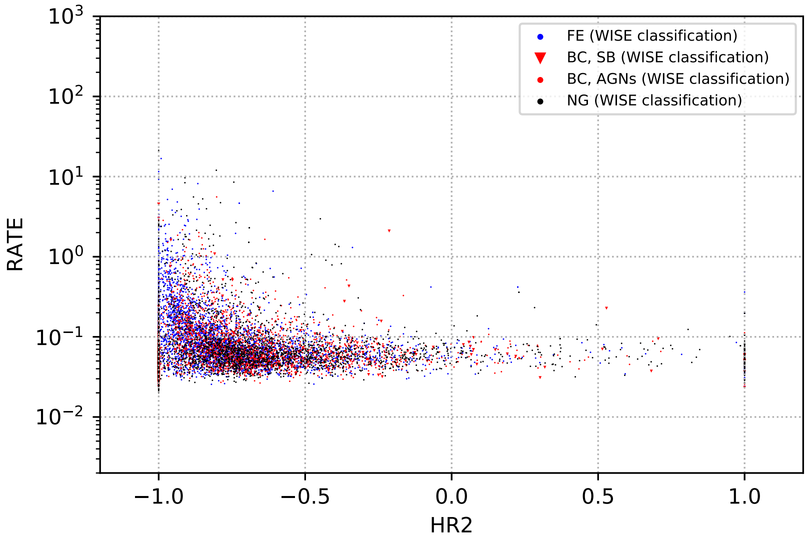

Fig. 3.10: X-ray count rate over HR2. The sources are highlighted according to the Wright et al. (2010) criteria in Tab. 3.3 and Fig. 3.4.

3.2.2 Counterparts in the Gaia Catalogue

The retrieved optical Gaia counterparts were checked on reliability by calculating the angular distance to the corresponding WISE counterpart. The 1-sigma positional error for each source can vary between 0.1” - 1.2” in the WISE catalogue. If the position of the Gaia match differed from the position of the WISE match by more than three times the 1-sigma positional error (≈ 3”), they were mostly likely not the same source. This was done via small-angle approximations and the equation for the distance between two points

$$\gamma = \sqrt{(\mathrm{Dec}_{WISE} - \mathrm{Dec}_{Gaia})^2 + (\mathrm{RA}_{Gaia} - \mathrm{RA}_{WISE})^2} \tag{3.3}$$

and all matches with an angular distance $\gamma < 3$ ” were classified as reliable. The rest was marked as unreliable as seen in Fig. 3.11. Furthermore, the different classes of candidates were separated according to the magnitudes of their WISE counterparts based on Wright et al. (2010).

Fig. 3.11 shows a linear correlation of the reliability of the matches which confirms the assumption that some Gaia counterparts don’t match the original sources. Those unreliable matches are marked in grey in every diagram that shows Gaia data and were not considered in further classification.

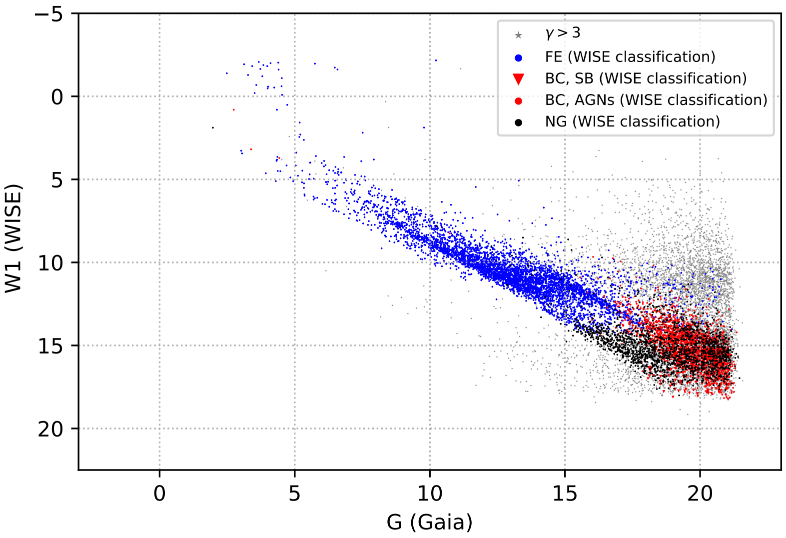

Fig. 3.11: Gaia and WISE magnitude diagram for counterpart comparison. The sources are highlighted according to the Wright et al. (2010) criteria in Tab. 3.3 and Fig. 3.4. Unreliable sources based on Eq. 3.3 were marked in grey.

The different classes of candidates were further separated according to their magnitude in the Gaia G band. Foreground candidates were narrowed down to those counterparts which had G magnitude of less than 12. Background candidates were narrowed down to those which had a G magnitude of more than 17. In general, it is visible that the blue foreground candidates appear brighter than the red background candidates and are grouped in different regions of the diagram in Fig. 3.12, Fig. 3.13, and also Fig. 3.14.

In the G-distance diagram in Fig. 3.13, also matches with an insufficient distance significance are marked. They did not fulfil the equation for

$$u = \sqrt{\chi^2/v} \tag{3.4}$$

according to Arenou et al. (2018) concerning the astrometric data where χ^2 is `astrometric_chi2_al` and v is `astrometric_n_good_obs_al-5`:

$$u < (1.2 \cdot \max(1, \exp(-0.2 \cdot (\mathrm{G} - 19.5)))) \tag{3.5}$$

They are also not used in the further analysis of Gaia data.

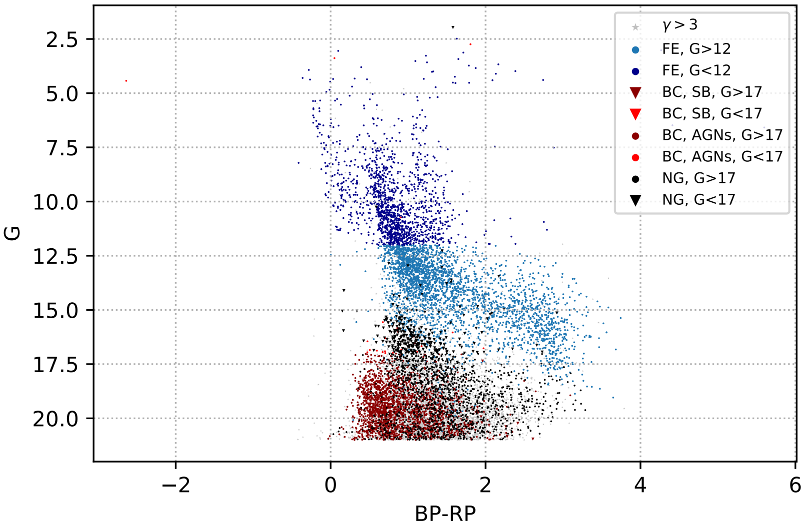

Fig. 3.12: Gaia colour magnitude diagram. The sources are highlighted according to the Wright et al. (2010) criteria in Tab. 3.3 and Fig. 3.4, and based on their G magnitude.

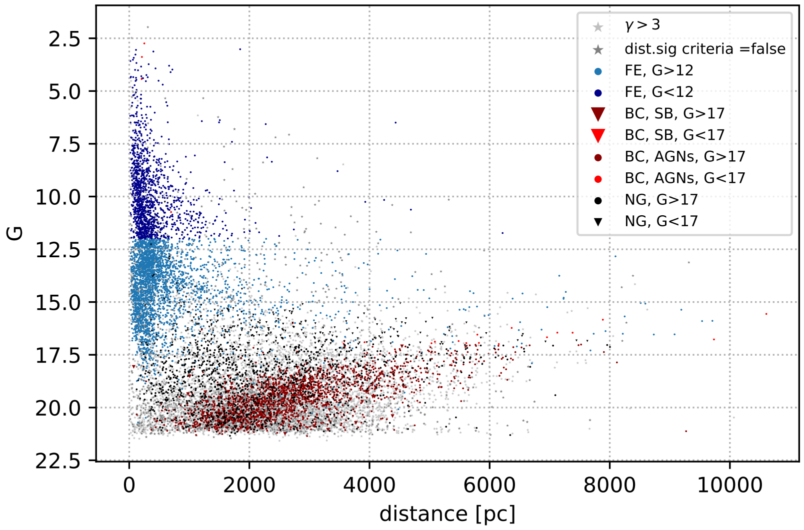

Fig. 3.13: Gaia G magnitude over estimated distance from the Gaia astrometry module. The sources are highlighted according to the Wright et al. (2010) criteria in Tab. 3.3 and Fig. 3.4, and based on their G magnitude.

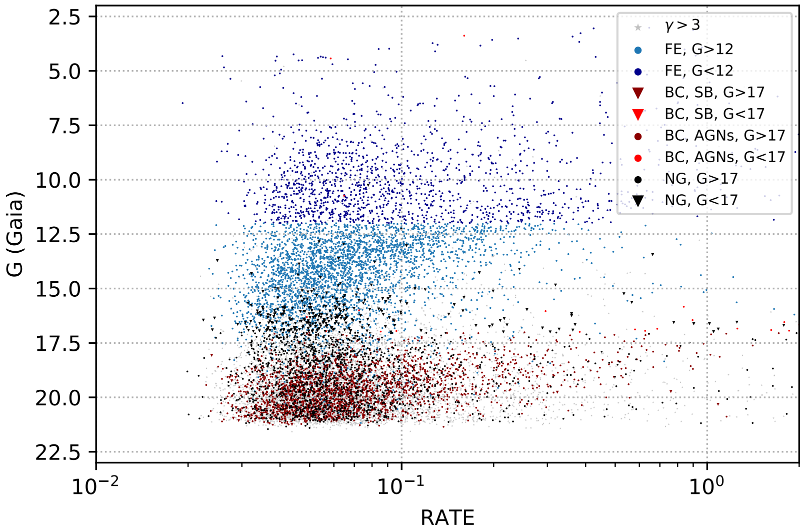

Fig. 3.14: Gaia G magnitude over eROSITA X-ray count rate. The sources are highlighted according to the Wright et al. (2010) criteria in Tab. 3.3 and Fig. 3.4, and based on their G magnitude.

3.2.3 Isochrones

Isochrones show the evolutionary tracks of stars and indicate the position of a stellar population in a colour-magnitude diagram depending on their age, metallicity and distance. Theoretical isochrones from the *Dartmouth Stellar Evolution Database* based on Dotter et al. (2007, 2008) were plotted in the magnitude diagrams to compare the detected sources in the field of view of Canis Major with theoretical values of galactic and Canis Major sources. As the stars of the Canis major dwarf galaxy are observed to be quite old, a certain amount of sources are expected to have turned off the main sequence and to be in the final stage of their stellar evolution as explained in section 2.1.

For the theoretical isochrones of the Canis Major population, a metallicity of $Z = 0.00658$, ages of $\tau = 2.5$ Gyr, $\tau = 7$ Gyr and $\tau = 15$ Gyr and distances of $d = 5.5$ kpc, $d = 7$ kpc and $d = 8.5$ kpc were chosen according to Martinez-Delgado et al. (2005).

For galactic foreground candidates, the metallicity $Z = 0.001925$ of the Sun was selected based on Vagnozzi (2019) to represent main sequence stars in our galactic neighbourhood. In order to cover most possible foreground sources, distances of $d = 10$ pc, $d = 100$ pc and $d = 400$ pc were plotted. To represent all populations in these distances, the age of the galactic foreground population was chosen as $\tau = 7.080$ Gyr as the median age of the solar and disc age. Based on Grady et al. (2020), ages of disc stars are at around $\tau = 10$ Gyr, while the age of the Sun is $\tau = 4.5$ Gyr according to Bonanno et al. (2002).

The extinction A for galactic populations was set to 0 as the objects are part of the Milky Way. The galactic extinction values of Canis Major in different wavelengths are taken from the NASA/IPAC Extragalactic Database based on Schlafly and Finkbeiner (2011) and can be found in Tab. 3.4. For Gaia magnitudes, no explicit values were available, so the next closest available wavelength was chosen.

Survey	g [mag]	r [mag]	J [mag]	K [mag]	BP [mag]	RP [mag]
Skymapper	0.872	0.603				
2MASS			0.187	0.080		
Gaia	0.542				0.753	0.409

Tab. 3.4: Galactic extinction values A for Canis Major from NASA/IPAC Extragalactic Database based on Schlafly and Finkbeiner (2011).

The expected apparent magnitudes m were calculated with the distance modulus via the absolute magnitude M, distance d plus an additional extinction correction factor A

$$m = M - [5 \cdot (1 - \log_{10}(d))] + A \tag{3.6}$$

and plotted as isochrone curves in the Skymapper (Fig. 3.16), Gaia (Fig. 3.19) and 2MASS (Fig. 3.22) colour-magnitude diagrams. The galactic isochrones fit well within a distinguishable main sequence.

Likely galactic foreground populations were marked in all available magnitude diagrams along a cut that was set at the line where foreground candidates were not any longer distinguishable from the other candidates and the theoretical Canis Major isochrones. The line equations are given in Tab. 3.5.

Survey	Cut
Skymapper	$g < (6.5 \cdot (g - r) + 12)$ $g < (-10.4 \cdot (g - r) + 23)$
2MASS	$K < (6.1 \cdot (J - K) + 10)$ $K < (-9.3 \cdot (J - K) + 19.2)$
Gaia	$G < (3.33 \cdot (BP - RP) + 11.67)$ $G < (-8.5 \cdot (BP - RP) + 27)$

Tab. 3.5: Criteria to determine galactic foreground populations in magnitude diagrams. The line equations of the cuts between foreground candidates and others are given in this table.

The Skymapper selection of likely foreground candidates was defined in Fig. 3.16 and highlighted in orange in the Gaia optical magnitude diagram in Fig. 3.18 and in the 2MASS magnitude diagram in Fig. 3.17. The coherency of different data sets was also checked in Fig. 3.15. The data of the *Padova database of stellar evolutionary tracks and isochrones* database[1] and *Dartmouth Stellar Evolution Database*[2] match as expected. As the *Dartmouth Stellar Evolution Database* provided data for all selected surveys, all isochrones were taken from there.

---

[1] `http://pleiadi.pd.astro.it/` (last visited on 11/04/2021)

[2] `http://stellar.dartmouth.edu/models/` (last visited on 11/04/2021)

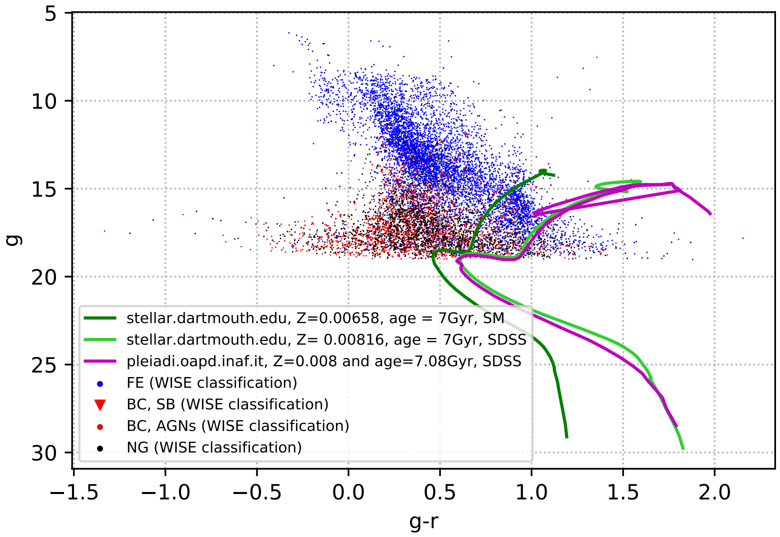

Fig. 3.15: Skymapper magnitudes with theoretical isochrones from two different data bases which indeed overlap. The sources are highlighted according to the Wright et al. (2010) criteria in Tab. 3.3 and Fig. 3.4.

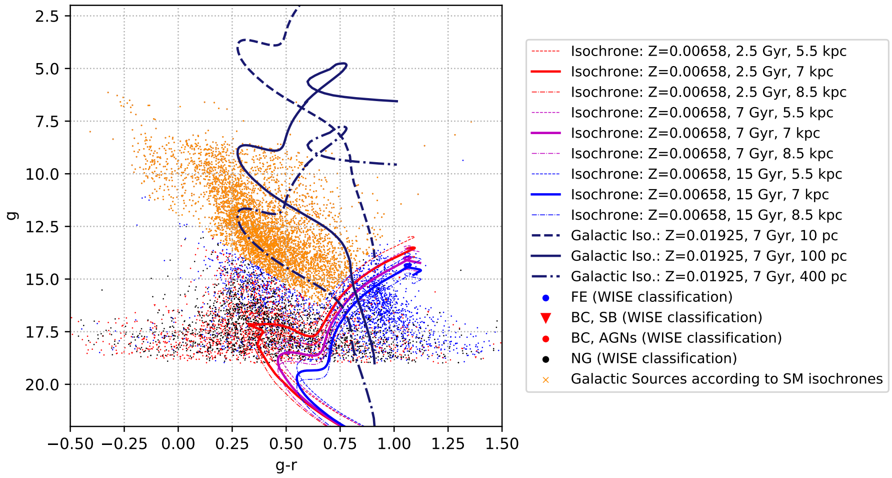

Fig. 3.16: Skymapper magnitude diagram with theoretical isochrones. Galactic sources based on Tab. 3.5. The sources are highlighted according to the Wright et al. (2010) criteria in Tab. 3.3 and Fig. 3.4.

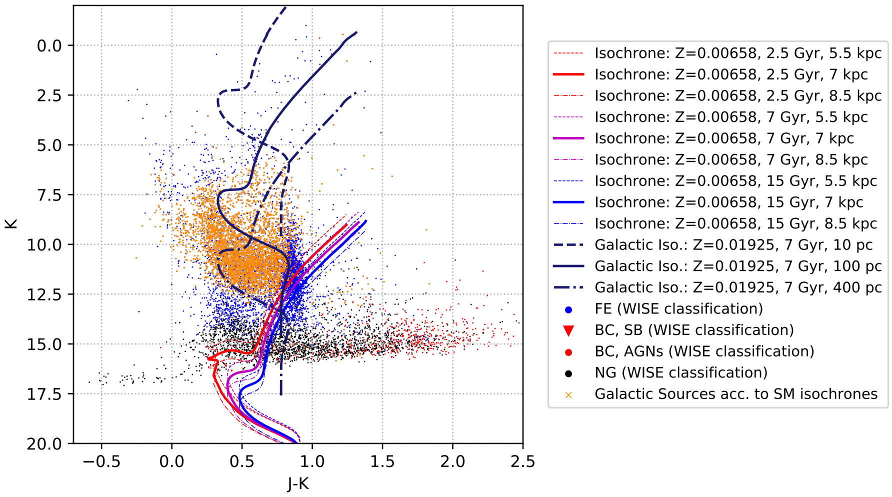

Fig. 3.17: 2MASS magnitude diagram with highlighted foreground candidates based on the Skymapper isochrone selection in Fig. 3.16. The sources are highlighted according to the Wright et al. (2010) criteria in Tab. 3.3 and Fig. 3.4.

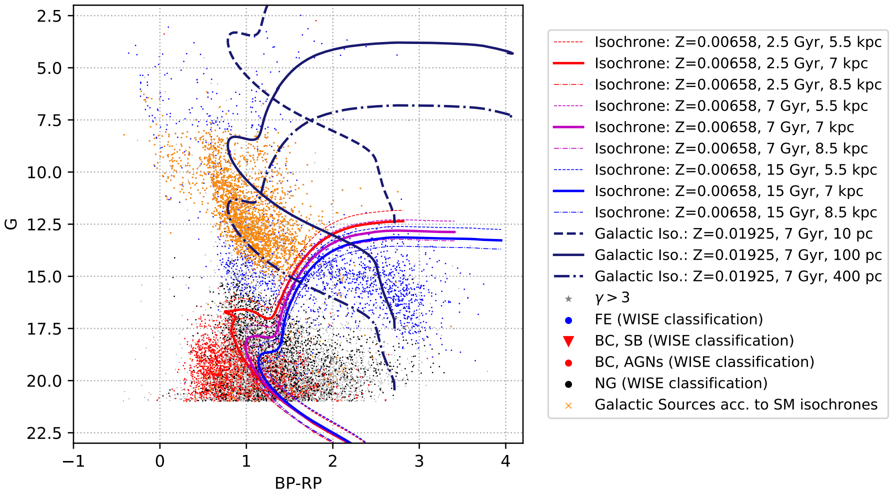

Fig. 3.18: Gaia magnitude diagram with highlighted foreground candidates based on the Skymapper isochrone selection in Fig. 3.16. The sources are highlighted according to the Wright et al. (2010) criteria in Tab. 3.3 and Fig. 3.4.

This procedure was repeated for the Gaia magnitudes. The likely galactic foreground population was marked in olive in the Gaia optical magnitude diagram in Fig. 3.19, and then highlighted in the magnitude diagrams of 2MASS in Fig. 3.20 and Skymapper in Fig. 3.21.

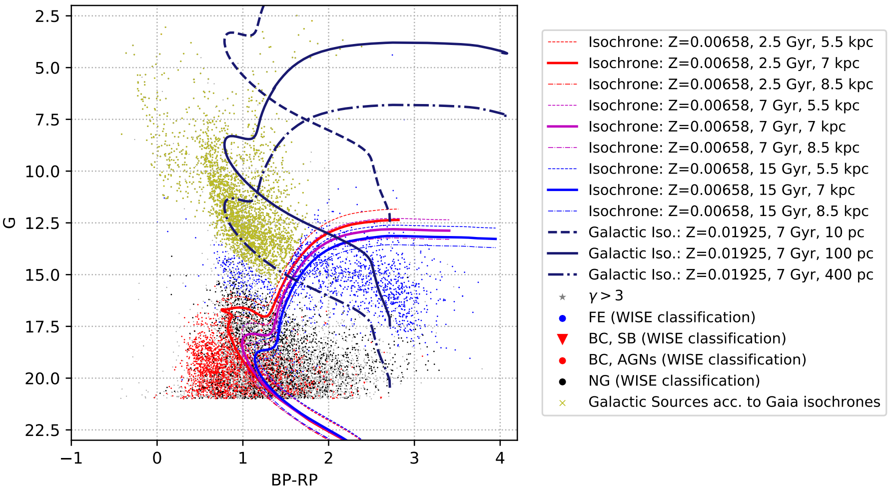

Fig. 3.19: Gaia magnitude diagram with theoretical isochrones. Galactic sources based on Tab. 3.5. The sources are highlighted according to the Wright et al. (2010) criteria in Tab. 3.3 and Fig. 3.4.

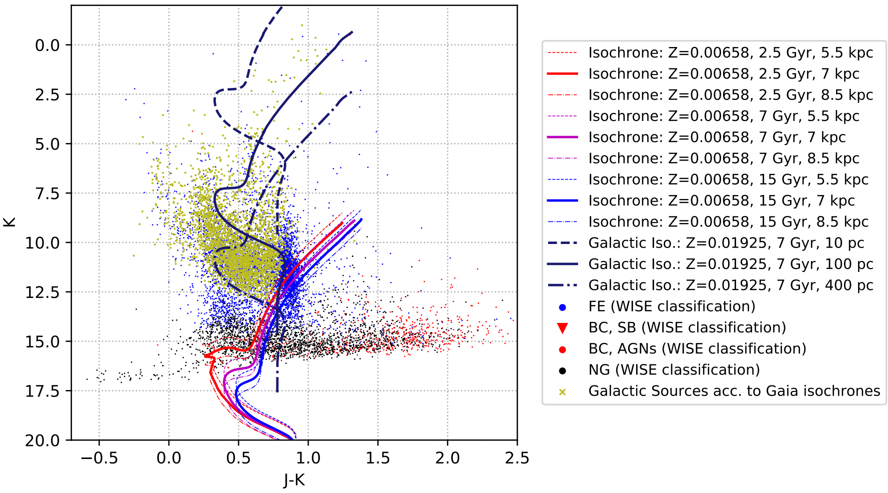

Fig. 3.20: 2MASS magnitude diagram with highlighted foreground candidates based on the Gaia isochrone selection in Fig. 3.19. The sources are highlighted according to the criteria in Tab. 3.3 and Fig. 3.4.

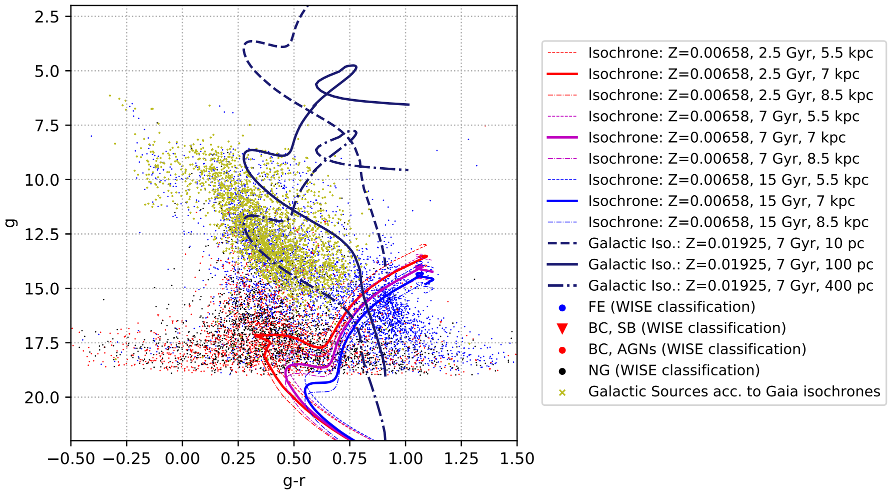

Fig. 3.21: Skymapper magnitude diagram with highlighted foreground candidates based on the Gaia isochrone selection in Fig. 3.19. The sources are highlighted according to the Wright et al. (2010) criteria in Tab. 3.3 and Fig. 3.4.

Lastly, the likely foreground population in the 2MASS magnitude diagram was identified in Fig. 3.22. This selection was then highlighted in green in the magnitude diagrams of Gaia in Fig. 3.23 and Skymapper in Fig. 3.24.

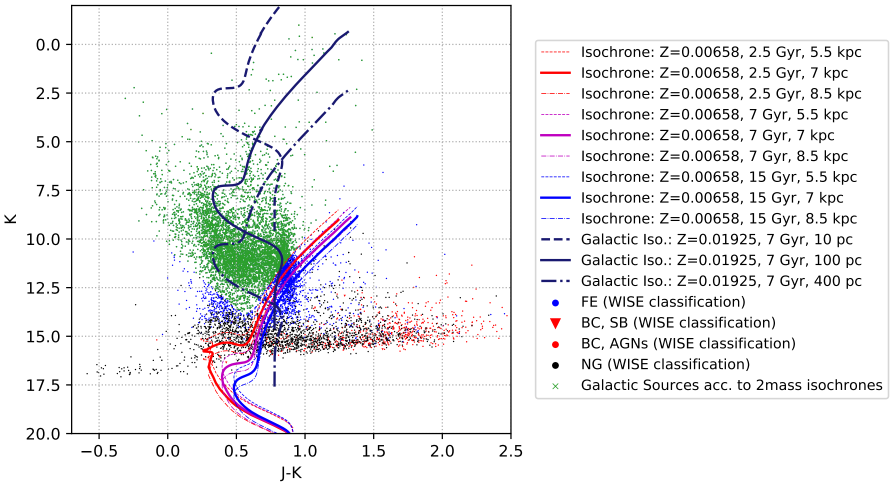

Fig. 3.22: 2MASS magnitude diagram with theoretical isochrones. Galactic sources based on Tab. 3.5. The sources are highlighted according to the Wright et al. (2010) criteria in Tab. 3.3 and Fig. 3.4.

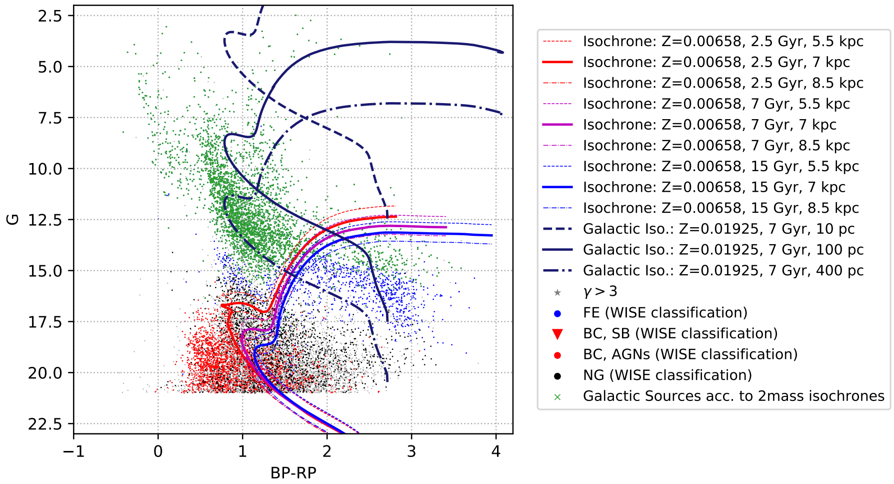

Fig. 3.23: Gaia magnitude diagram with highlighted foreground candidates based on the 2MASS isochrone selection in Fig. 3.22. The sources are highlighted according to the Wright et al. (2010) criteria in Tab. 3.3 and Fig. 3.4.

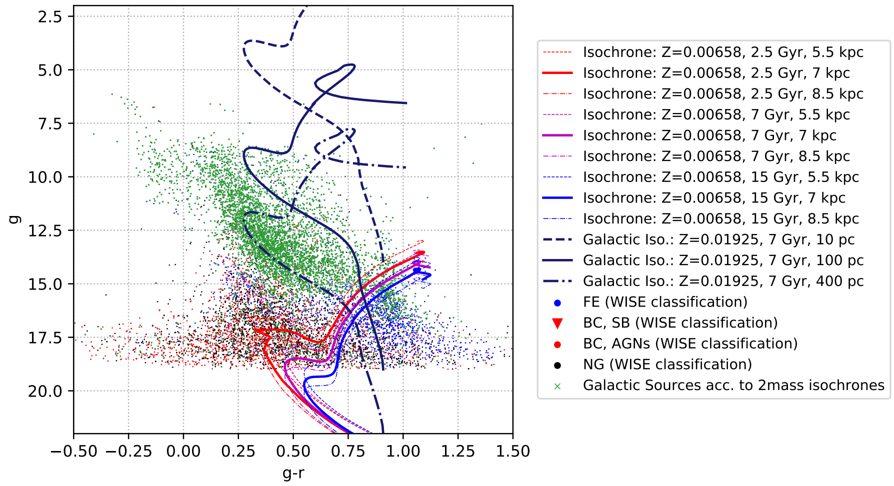

Fig. 3.24: Skymapper magnitude diagram with highlighted foreground candidates based on the 2MASS isochrone selection in Fig. 3.22. The sources are highlighted according to the Wright et al. (2010) criteria in Tab. 3.3 and Fig. 3.4.

The comparison of foreground candidate selections of the different surveys concludes that the selections are mostly focused on the same region in every magnitude diagram. All selected galactic candidates lie in the upper part of the main sequence which supports the theory of them being foreground stars. This is observable in all magnitude diagrams and therefore these counterparts are very likely to be foreground objects. But, there is one noticeable aberration in the 2MASS colour-colour diagrams. The selection of foreground candidates based on the 2MASS isochrones in Fig. 3.22 is not completely in accordance with the selection based on Skymapper and Gaia isochrones in Fig. 3.17 and 3.20 as the selections based on Gaia and Skymapper both do not include sources above J-K bigger than approximately 0.8 mag. Henceforth, the Skymapper isochrone criteria in Tab. 3.5 will be used to identify foreground candidates in 2MASS diagrams as this selection appears more precise than the one based on the 2MASS isochrones.

3.2.4 2MASS Criteria

Martin et al. (2004) identified two areas of Canis Major population in 2MASS data as seen in Tab. 3.6, the Giant Branch which is explained in section 2.1, and the Red Clump. Red Clump stars are low-mass stars in their core-helium-burning stage and form a notably prominent cluster next to the red giant branch. The sources identified as part of the Giant Branch and Red Clump by this criteria were marked in the 2MASS magnitude diagram in Fig. 3.25 and plotted in diagrams of eROSITA data. The X-ray count rate over the two hardness ratios can be found in Fig. 3.26 and Fig. 3.27. The hardness ratio diagram is in Fig. 3.28. These diagrams don't provide a lot of new insights. The sources appear to be mostly soft X-ray sources based on their mostly positive HR1, and mainly negative HR2. The hardness ratio diagram in Fig. 3.28 still shows only a slight correlation with the hardness ratio models and suggests that most sources are thermal emitting as indicated by the green APEC model with a low temperature (kT around 0.2 to 1 keV) and low absorption as discussed earlier in section 3.2.1.

Class	J-K [mag] Criteria	K [mag] Criteria
Giant Branch	$0.807 < \text{J-K} < 1.307$	$8.08 < \text{K} < 12.08$
Red Clump	$0.657 < \text{J-K} < 0.757$	$12.08 < \text{K} < 13.58$

Tab. 3.6: Martin et al. (2004) selection of Canis Major sources respecting the galactic extinction from Tab. 3.4 which was corrected in the paper but not in the data used here.

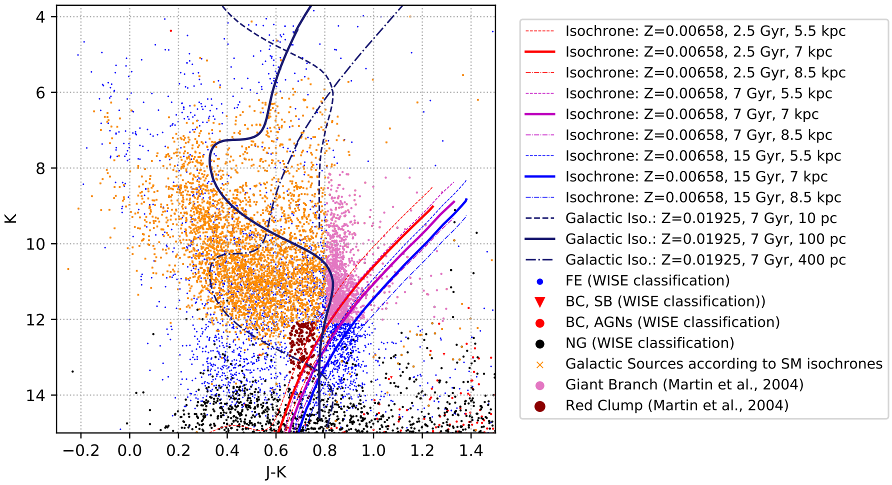

Fig. 3.25: 2MASS magnitude diagram with theoretical Canis Major isochrones and the selection of Martin et al. (2004) (Tab. 3.25) marked in pink. The rest of the sources are marked based on Tab. 3.3 and Fig. 3.4.

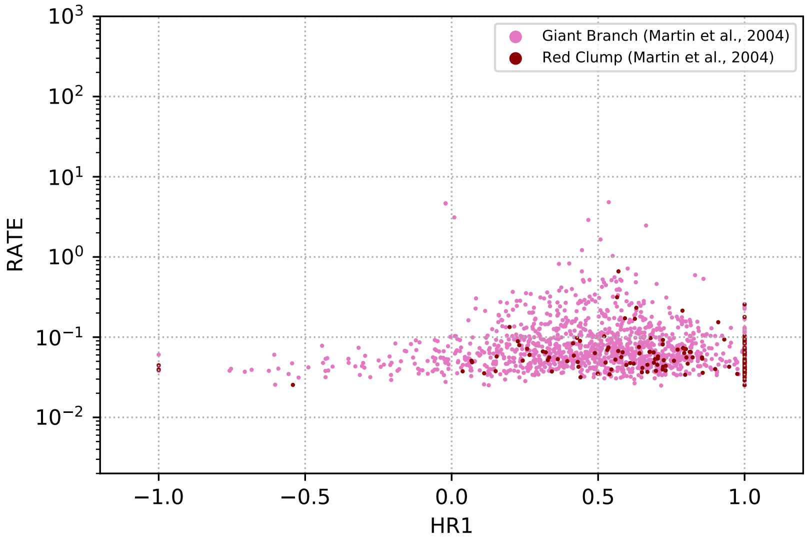

Fig. 3.26: RATE over HR1 diagram with only the matches meeting the Canis Major criteria from Tab. 3.6.

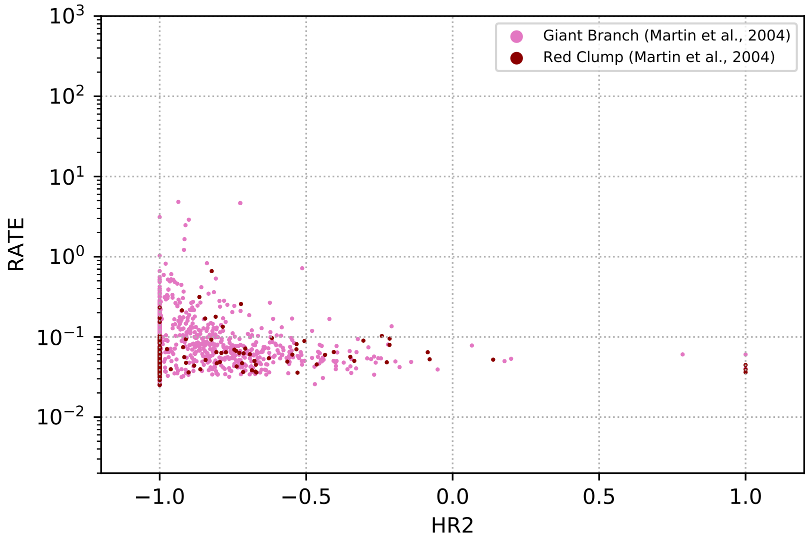

Fig. 3.27: RATE over HR2 diagram with only the matches meeting the Canis Major criteria in Tab. 3.6.

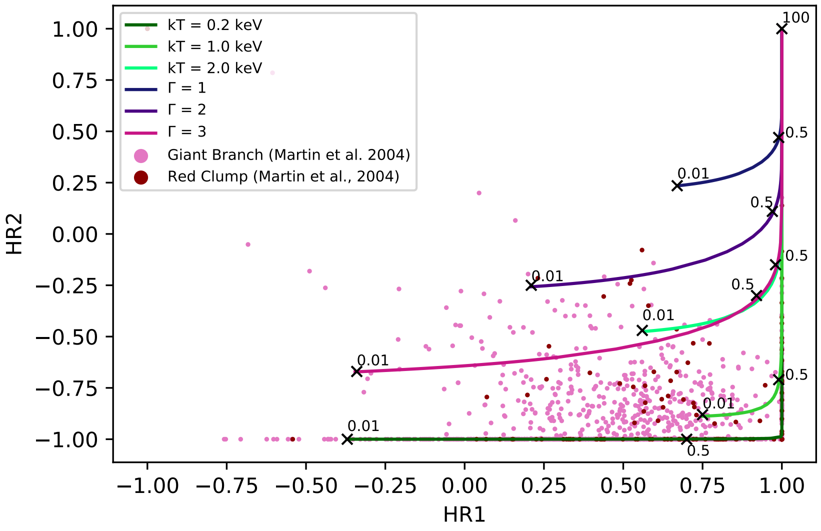

Fig. 3.28: HR diagram with hardness ratio models and only the matches meeting the Canis Major criteria in Tab. 3.6. Models are the same as Fig. 3.8. Column densities (N_H) are marked by crosses and value in 10^{22} cm^{-2}. Median errors on HR1 and HR2 are 0.26 and 0.23 respectively.

3.2.5 Analysis of X-Ray Properties

From the selection in section 3.2.4, five of the nine brightest sources were picked for further analysis. Sara Saeedi provided a spectral analysis of eROSITA data where the spectrum for each source was extracted and fitted with a spectral model. This method made it possible to find the conversion factor between the count rate measured with eROSITA and the real flux of the source. The energy conversion factor (ECF) was computed by using Eq. 3.7 from Saeedi et al. (2016). With the ECF, it was possible to calculate the estimated flux

$$F_x = \frac{RATE}{ECF} \tag{3.7}$$

for all sources. The ECF values of the sources in Tab. 3.7 were averaged and yielded a value of ECF = 3.46e11. The spectral analysis by Sara Saeedi suggests that sources 4, 5 and 7 are foreground stars, 6 and 8 are unclear.

Number	Net count rate (cts/s)	Flux (0.2–5.0 keV)
4	1.636	4.6931e-12
5	2.4931	6.9505e-12
7	1.348	4.1138e-12

Tab. 3.7: Sources used for ECF calculation.

Next, the X-ray-to-optical flux ratio

$$\log\left(\frac{F_x}{F_{opt}}\right) = \log_{10}(F_x) + \frac{m_1 + m_2}{2 \cdot 2.5} + 5.37 \tag{3.8}$$

was calculated according to Saeedi et al. (2016) to separate optically bright sources from bright X-ray sources. The equation was slightly modified by replacing the SDSS9 bands with m_1 and m_2, where m_1 refers to the g band in Skymapper and BP in Gaia, and m_2 refers to the Skmapper r band and Gaia RP band respectively. The X-ray-to-optical flux ratio as function of the hardness ratios can be found in Fig. 3.29 and Fig. 3.30 for Skymapper magnitudes, and Fig. 3.31 and Fig. 3.32 for Gaia magnitudes.

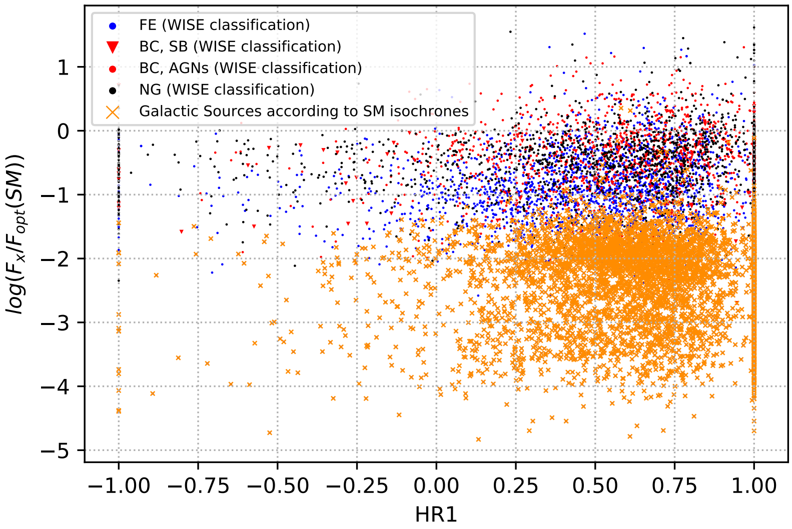

Fig. 3.29: X-ray-to-optical flux ratio for all eROSITA-SM counterparts. The sources are highlighted according to the Wright et al. (2010) criteria in Tab. 3.3 and Fig. 3.4 and to the isochrone criteria in Fig. 3.16.

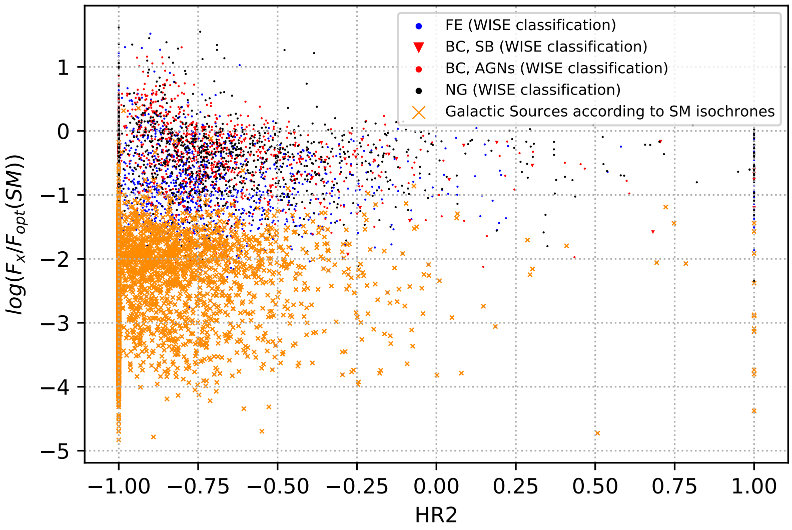

Fig. 3.30: X-ray-to-optical flux ratio for all eROSITA-SM counterparts. The sources are highlighted according to the Wright et al. (2010) criteria in Tab. 3.3 and Fig. 3.4 and to the isochrone criteria in Fig. 3.16.

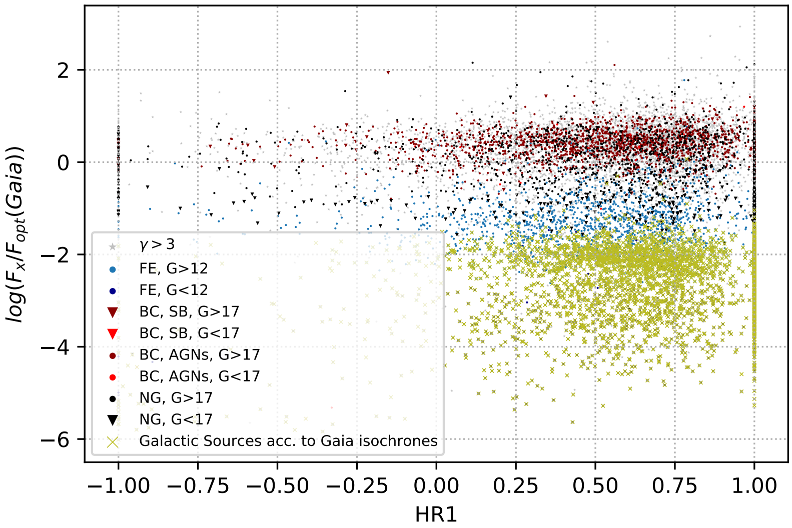

Fig. 3.31: X-ray-to-optical flux ratio for all eROSITA-Gaia counterparts. The sources are highlighted according to the Wright et al. (2010) criteria in Tab. 3.3 and Fig. 3.4 and to the isochrone criteria in Fig. 3.19.

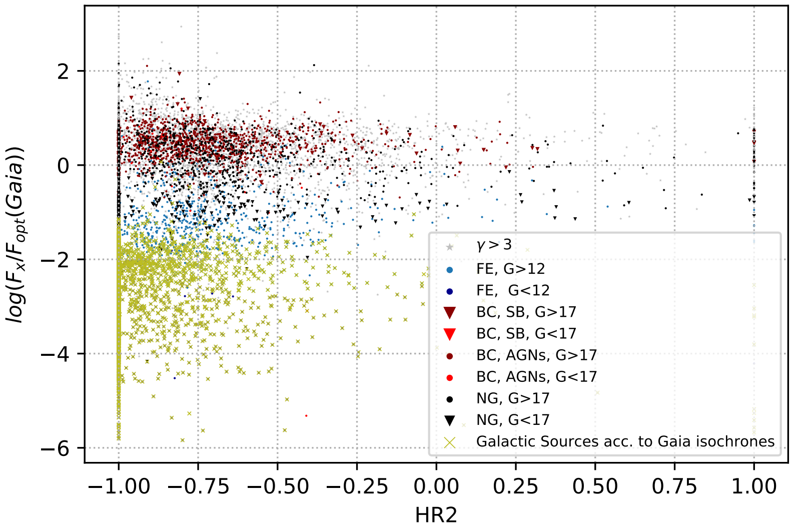

Fig. 3.32: X-ray-to-optical flux ratio for all eROSITA-Gaia counterparts. The sources are highlighted according to the Wright et al. (2010) criteria in Tab. 3.3 and Fig. 3.4 and to the isochrone criteria in Fig. 3.19.

In order to get the error on the flux ratio, the error on the RATE, which is defined as

$$RATE = \frac{B_0}{exposure} \tag{3.9}$$

had to be calculated :

$$\triangle RATE = \sqrt{\left(\frac{1}{exposure}\right)^2 \cdot EB_0^2} = \sqrt{\left(\frac{RATE}{B_0}\right)^2 \cdot EB_0^2}. \tag{3.10}$$

with the total counts B_0, and their corresponding errors EB_0 for the error of the RATE. Including the error of the magnitudes $\triangle m_i$, the error on the X-ray-to-optical flux ratio added up to:

$$\triangle \log\left(\frac{F_x}{F_{opt}}\right) = \sqrt{\left(\frac{1}{\ln(10) \cdot RATE}\right)^2 \cdot \triangle RATE^2 + \frac{1}{25}\triangle m_1^2 + \frac{1}{25} \cdot \triangle m_2^2} \tag{3.11}$$

The error bars of the X-ray-to-optical flux ratio can be found in Fig. 3.33. To get a hint of the dimension of the hardness ratio errors, Fig. 3.34 shows the hardness ratio diagram of likely Canis Major sources with corresponding error bars as calculated in Eq. 3.2. The errors of the hardness ratio vary a lot and should be closer considered in further work with specific sources. The median error on HR1 is 0.26, the median error on HR2 is 0.23.

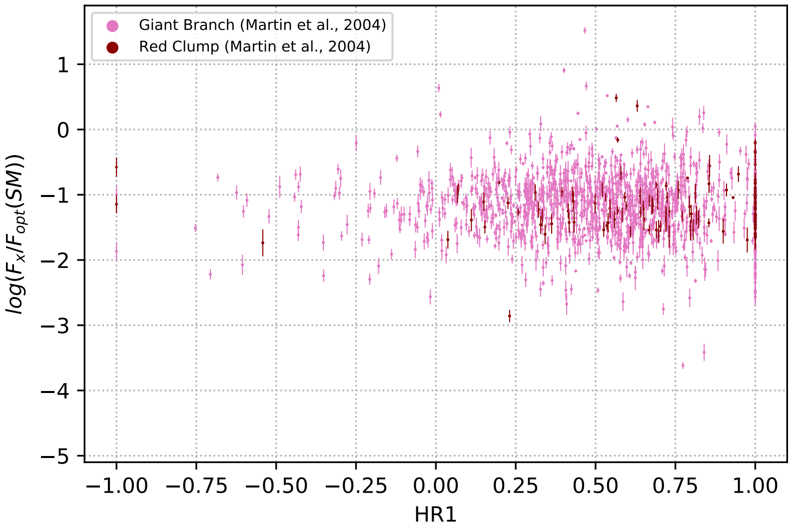

Fig. 3.33: X-ray-to-optical flux ratio for eROSITA-Skymapper data and likely Canis Major sources according to Tab. 3.25 with error bars for the flux-ratio.

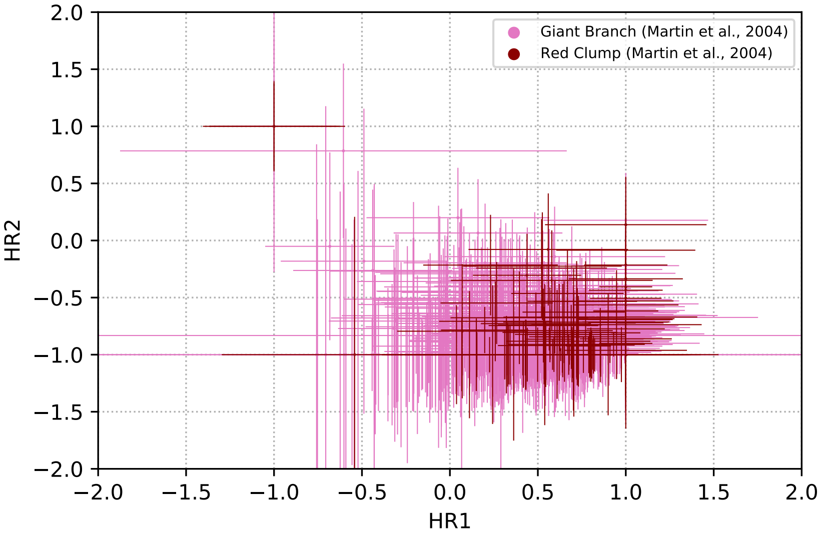

Fig. 3.34: Hardness Ratio diagram of likely Canis Major sources according to Tab. 3.25 with error bars. The median values of the errors on HR1 and HR2 are 0.26 and 0.23 respectively.

Fig. 3.33 shows that the Canis Major sources appear to be distributed around $\log\left(\frac{F_x}{F_{opt}}\right) = -1$ in comparison to Skymapper optical magnitudes. Background sources like X-ray binaries are at $\log\left(\frac{F_x}{F_{opt}}\right) = 0$ in Fig. 3.36 and Fig. 3.37 because they are bright in X-ray.
On the other hand, galactic foreground sources like stars can be found below $\log\left(\frac{F_x}{F_{opt}}\right) = -2$ in Fig. 3.35. They are less bright in X-ray but especially bright in optical magnitudes which supports the foreground star theory for those counterparts.

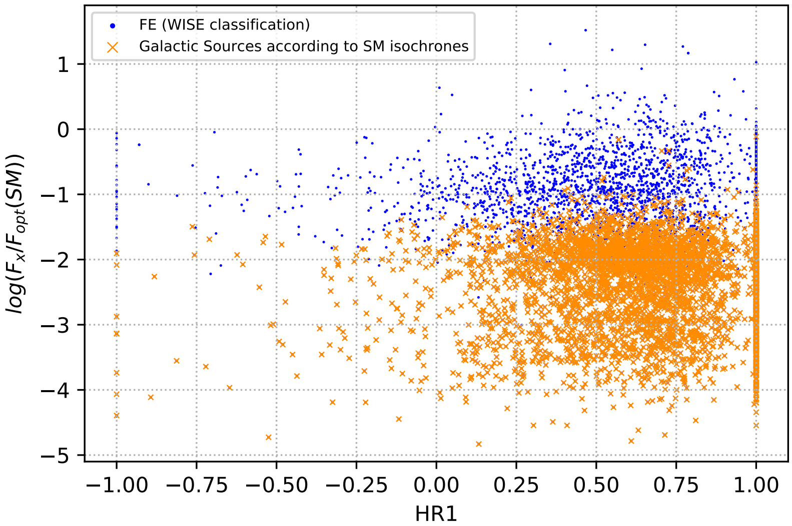

Fig. 3.35: X-ray-to-optical flux ratio for foreground candidates of eROSITA-SM data. The sources are highlighted according to the WISE criteria in Tab. 3.3 and Fig. 3.4 and to the isochrone criteria in Fig. 3.16.

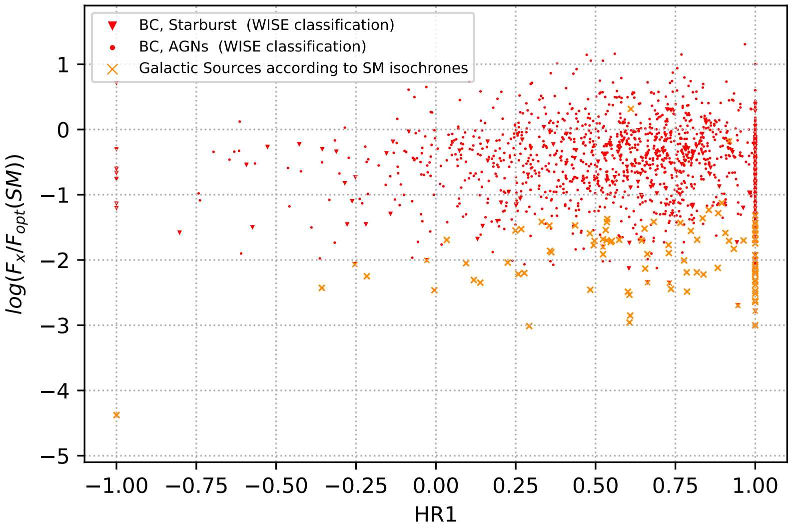

Fig. 3.36: X-ray-to-optical flux ratio for background candidates of eROSITA-SM data. The sources are highlighted according to the WISE criteria in Tab. 3.3 and Fig. 3.4 and to the isochrone criteria in Fig. 3.16.

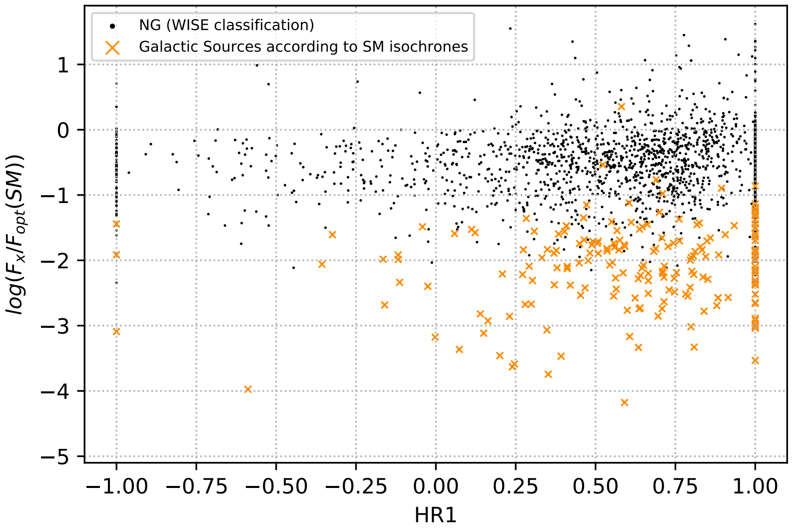

Fig. 3.37: X-ray-to-optical flux ratio for Normal Galaxy candidates of eROSITA-SM data. The sources are highlighted according to the WISE criteria in Tab. 3.3 and Fig. 3.4 and to the isochrone criteria in Fig. 3.16.

3.3 Final Classification

The final step in the population study of the Canis Major dwarf spheroidal galaxy is combining the results from the previous analysis. In order to do this, the selected sources from Martin et al. (2004) in section 3.2.4 were singled out and further analysed by the WISE, Gaia and isochrone criteria. Canis Major candidates were marked in the following diagrams by dots, foreground candidates by crosses.

The selected sources were plotted in X-ray-to-optical flux ratio diagrams as introduced in section 3.2.5. Foreground candidates were located below $\log\left(\frac{F_x}{F_{opt}}\right) = -2$, while Canis Major candidates were situated around $\log\left(\frac{F_x}{F_{opt}}\right) = -1$. This pattern can also be observed in the selection of Martin et al. in Fig. 3.38 to Fig. 3.41 where clear foreground star candidates can be found in the lower part of the diagram due to their brightness in optical magnitudes.

From the first and most helpful WISE classification in section 3.2.1, a lot of conclusions could be drawn. The WISE classification identified background (BC), foreground stars and elliptical galaxies (FE) and normal galaxy (NG) candidates and were marked accordingly in the final selection. Most counterparts in Fig. 3.38 to Fig. 3.41 belong to the foreground stars and elliptical galaxies class which is in accordance with the position and type of the Canis Major galaxy.

The isochrone criteria from section 3.2.3 was used to highlight high probability foreground candidates. Orange crosses in Fig. 3.38 and in Fig. 3.39 mark foreground candidates that were derived from the position of the theoretical isochrones in the Skymapper colour-magnitude diagram in Fig. 3.16. Green crosses in Fig. 3.40 and in Fig. 3.41 were taken from the optical Gaia isochrones in Fig. 3.19. These sources lie above the intersection with the Canis Major isochrones on the main sequence of the optical colour-magnitude diagrams. Thus, they qualify as highly likely foreground candidates and won't be taken in the final selection of Canis Major candidates.

Another criteria which can be considered through counterparts from the Gaia catalogue is the value of magnitude. In section 3.2.2, it was discussed that Gaia matches with a G-magnitude of less than 12 are very likely foreground candidates. These counterparts were marked as light blue crosses in Fig. 3.40 and 3.41, and also not considered as Canis Major sources.

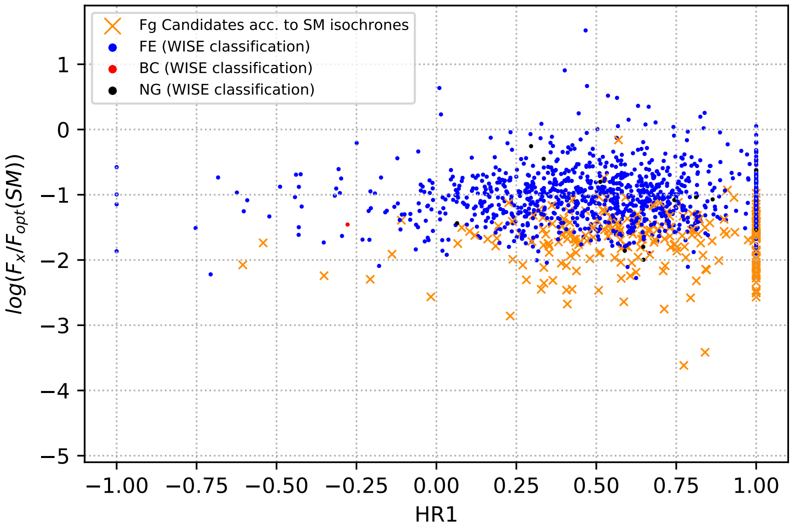

Fig. 3.38: X-ray-to-optical flux ratio for eROSITA-SM data and likely Canis Major sources. The sources are highlighted according to the WISE criteria in Tab. 3.3 and Fig. 3.4 and to the isochrone criteria in Fig. 3.16.

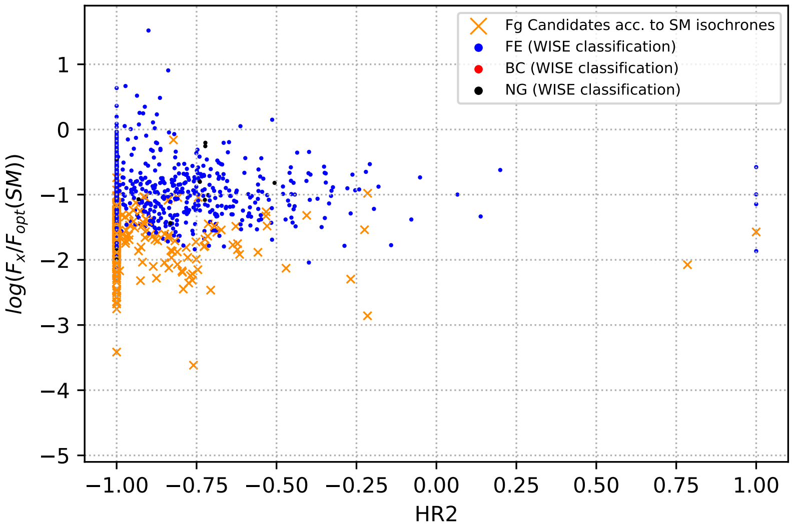

Fig. 3.39: X-ray-to-optical flux ratio for eROSITA-SM data and likely Canis Major sources. The sources are highlighted according to the WISE criteria in Tab. 3.3 and Fig. 3.4 and to the isochrone criteria in Fig. 3.16.

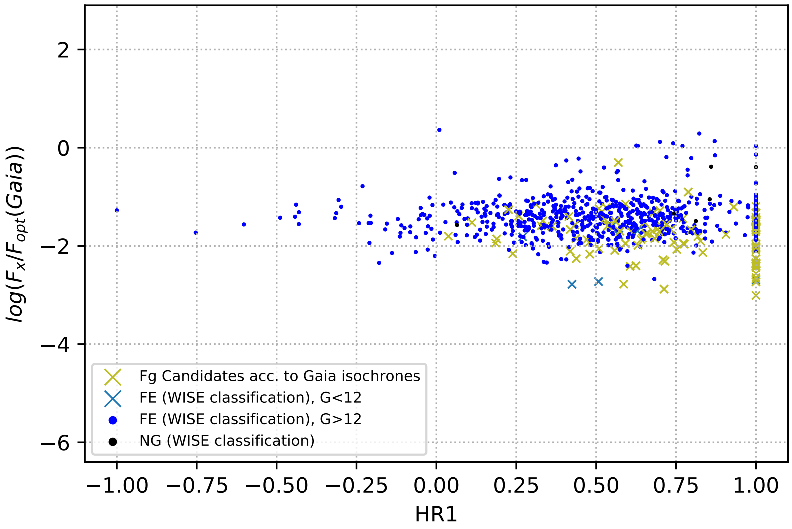

Fig. 3.40: X-ray-to-optical flux ratio for eROSITA-Gaia data and likely Canis Major sources. The sources are highlighted according to the WISE criteria in Tab. 3.3 and Fig. 3.4 and to the isochrone criteria in Fig. 3.19.

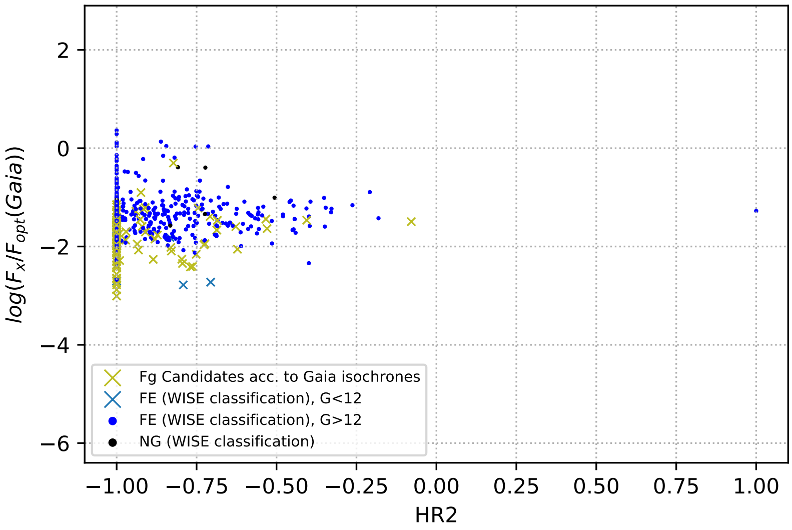

Fig. 3.41: X-ray-to-optical flux ratio for eROSITA-Gaia data and likely Canis Major sources. The sources are highlighted according to the WISE criteria in Tab. 3.3 and Fig. 3.4 and to the isochrone criteria in Fig. 3.19.

By excluding the likely foreground candidates which were identified in this section, a selection of 1 289 Canis Major candidates can be created based on the remaining counterparts. Those sources were marked as blue dots in Fig. 3.38 to Fig. 3.41. Fig. 3.42 depicts the remaining Canis Major candidates in a hardness ratio diagram. As most sources lie in the bottom right of the diagram, this suggests a thermal emission with low temperatures as seen as the dark green APEC model, and low absorption values as seen by the low N_H values.

In conclusion, it can be said that the selection of Martin et al. (2004) shows promising Canis Major candidates in the eROSITA data which can be further analysed in future works.

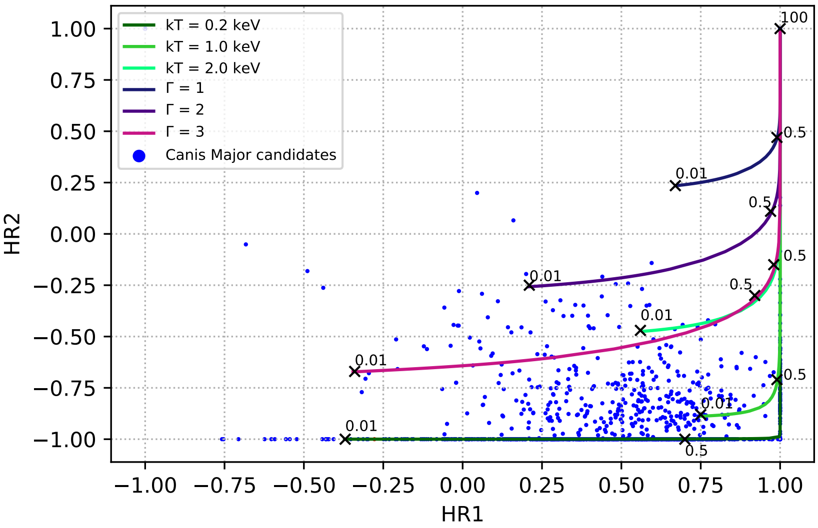

Fig. 3.42: Hardness ratio diagram with hardness ratio models and the final Canis Major candidates. Models are the same as Fig. 3.8. Column densities (N_H) are marked by crosses and value in 10^{22} cm^{-2}. The median values of the errors on HR1 and HR2 are 0.26 and 0.23 respectively.

4 Conclusion

This first look at the data of eRASS1 shows potential for further analysis of data concerning the Canis Major dwarf spheroidal galaxy.

From the original 17 676 X-ray sources in the region of the Canis Major galaxy, most could be narrowed down to background and foreground candidates based on various criteria. The first criteria was based on Wright et al. (2010) and provided four classification types from the WISE magnitudes: Galactic Foreground Sources and Elliptical Galaxies (FE), Starburst Galaxies (SB), Active Galactic Nuclei (AGN), and Normal Galaxies (NG). Next, Gaia counterparts were distinguished through their magnitudes and comparable WISE matches. Through theoretical isochrones, galactic foreground populations were identified. Subsequently, a closer look was taken at a selection by Martin et al. (2004) which identified Canis Major sources in the 2MASS magnitudes diagram. This selection was narrowed down by the previous criteria to 1 289 likely Canis Major candidates. In combination with the hardness ratio models, most candidates seem to have thermal emission with low temperature and low absorption. The thereby as Canis Major candidates identified sources from section 3.3 are in agreement with previous findings of Martin et al. (2004) and should be further analysed in future research to gain more detailed information about the X-ray sources of the Canis Major galaxy. Especially an extended spectral analysis would be helpful as there hasn't been a lot of previous research in this area. Through this, a better understanding of the population and formation of the Canis Major dwarf galaxy could be achieved.

In addition to new insights to the population of the Canis Major galaxy, conclusions regarding the utility of the eROSITA data were drawn. An important result is that the standard bands of eROSITA are not useful for hardness ratio-based analysis as seen in Fig. 3.8 and need to be adjusted for better comparability. In anticipation of the next seven eROSITA data releases, more discoveries and milestones will hopefully be reached in X-ray astronomy, and regarding the Canis Major dwarf spheroidal galaxy.

References

Arenou, F. et al. (2018). “Gaia Data Release 2 - Catalogue validation”. In: *A&A* 616, A17. DOI: `10.1051/0004-6361/201833234`.

Bonanno, A. et al. (2002). “The age of the Sun and the relativistic corrections in the EOS”. In: *A&A* 390.3, pp. 1115–1118. DOI: `10.1051/0004-6361:20020749`.

Cutri, R. M. et al. (2014). “VizieR Online Data Catalog: AllWISE Data Release (Cutri+ 2013)”. In: *VizieR Online Data Catalog*, II/328, pp. II/328.

Dotter, A. et al. (2007). “The ACS Survey of Galactic Globular Clusters. II. Stellar Evolution Tracks, Isochrones, Luminosity Functions, and Synthetic Horizontal-Branch Models”. In: *The Astronomical Journal* 134.1, pp. 376–390. DOI: `10.1086/517915`.

Dotter, A. et al. (2008). “The Dartmouth Stellar Evolution Database”. In: *The Astrophysical Journal Supplement Series* 178.1, pp. 89–101. DOI: `10.1086/589654`.

ESO (2007). *Hertzsprung-Russell Diagram.* URL: `https://www.eso.org/public/images/eso0728c/` (visited on 02/04/2021).

Gaia Collaboration et al. (2016). “The Gaia mission”. In: *A&A* 595, A1. DOI: `10.1051/0004-6361/201629272`.

Gaia Collaboration et al. (2018). “Gaia Data Release 2 - Summary of the contents and survey properties”. In: *A&A* 616, A1. DOI: `10.1051/0004-6361/201833051`.

Grady, J. et al. (2020). “Age demographics of the Milky Way disc and bulge”. In: *Monthly Notices of the Royal Astronomical Society* 492.3, pp. 3128–3142. DOI: `10.1093/mnras/stz3617`.

Karttunen, H. et al. (2017). *Fundamental Astronomy.* 6th ed. Springer-Verlag Berlin Heidelberg. ISBN: 978-3-662-53045-0.

Martin, N. F. et al. (2004). “A dwarf galaxy remnant in Canis Major: the fossil of an in-plane accretion on to the Milky Way”. In: *Monthly Notices of the Royal Astronomical Society* 348.1, pp. 12–23. DOI: `10.1111/j.1365-2966.2004.07331.x`.

Martinez-Delgado, D. et al. (2005). “The Closest View of a Dwarf Galaxy: New Evidence on the Nature of the Canis Major Overdensity”. In: *The Astrophysical Journal* 633.1, pp. 205–209. DOI: `10.1086/432635`. URL: `https://doi.org/10.1086/432635`.

McConnachie, A. W. (2012). “The Observed Properties of Dwarf Galaxies in and around the Local Group”. In: *The Astronomical Journal* 144.1, p. 4. DOI: `10.1088/0004-6256/144/1/4`.

Merloni, A. et al. (2012). “eROSITA Science Book: Mapping the Structure of the Energetic Universe”. In: *arXiv e-prints*. arXiv: `1209.3114`.

MPE (2020a). *eROSITA finds large-scale bubbles in the halo of the Milky Way.* URL: `https://www.mpe.mpg.de/7540556/news20201210?c=260780` (visited on 11/04/2021).

– (2020b). *Our deepest view of the X-ray sky.* URL: `https://www.mpe.mpg.de/7461761/news20200619` (visited on 02/04/2021).

Predehl, P. et al. (2021). “The eROSITA X-ray telescope on SRG”. In: *A&A* 647, A1. DOI: `10.1051/0004-6361/202039313`.

Saeedi, S. et al. (2016). “XMM-Newton study of the Draco dwarf spheroidal galaxy”. In: *A&A* 586, A64. DOI: `10.1051/0004-6361/201526233`.

Salvato, M. et al. (2017). “Finding counterparts for all-sky X-ray surveys with Nway: a Bayesian algorithm for cross-matching multiple catalogues”. In: *Monthly Notices of the Royal Astronomical Society* 473.4, pp. 4937–4955. DOI: `10.1093/mnras/stx2651`.

Schlafly, E. F. and D. P. Finkbeiner (2011). “Measuring Reddening with Sloan Digital Sky Survey Stellar Spectra and Recalibrating SFD”. In: *The Astrophysical Journal* 737.2, p. 103. DOI: `10.1088/0004-637x/737/2/103`.

Skrutskie, M. F. et al. (2006). “The Two Micron All Sky Survey (2MASS)”. In: *The Astronomical Journal* 131.2, pp. 1163–1183. DOI: `10.1086/498708`.

Vagnozzi, S. (2019). “New Solar Metallicity Measurements”. In: *Atoms* 7.2. DOI: `10.3390/atoms7020041`.

Wolf, C. et al. (2018). “SkyMapper Southern Survey: First Data Release (DR1)”. In: *Publications of the Astronomical Society of Australia* 35, e010. DOI: `10.1017/pasa.2018.5`.

Wright, E. L. et al. (2010). “The Wide-field Infrared Survey Explorer (WISE): Mission Description and Initial on-Orbit Performance”. In: *The Astronomical Journal* 140.6, pp. 1868–1881. DOI: `10.1088/0004-6256/140/6/1868`.

Acknowledgements

I want to thank everyone who supported me during my time writing this bachelor's thesis. Thanks to my supervisor Manami Sasaki for the interesting topic and support. Thank you to Sara Saeedi for you help with my questions and providing the hardness ratio models and spectral analysis. Thanks to Jonathan Knies for artemis and taking care of my struggles with it. I also want to thank Katharina and Dominik for their support with the isochrones, Steven for his general assistance, and Roman and Clarissa for mutual motivation for our theses.

This work is based on data from eROSITA, the primary instrument aboard SRG, a joint Russian-German science mission supported by the Russian Space Agency (Roskosmos), in the interests of the Russian Academy of Sciences represented by its Space Research Institute (IKI), and the Deutsches Zentrum für Luft- und Raumfahrt (DLR). The SRG spacecraft was built by Lavochkin Association (NPOL) and its subcontractors, and is operated by NPOL with support from the Max Planck Institute for Extraterrestrial Physics (MPE). The development and construction of the eROSITA X-ray instrument was led by MPE, with contributions from the Dr. Karl Remeis Observatory Bamberg & ECAP (FAU Erlangen-Nuernberg), the University of Hamburg Observatory, the Leibniz Institute for Astrophysics Potsdam (AIP), and the Institute for Astronomy and Astrophysics of the University of Tübingen, with the support of DLR and the Max Planck Society. The Argelander Institute for Astronomy of the University of Bonn and the Ludwig Maximilians Universität Munich also participated in the science preparation for eROSITA. The eROSITA data shown here were processed using the eSASS/NRTA software system developed by the German eROSITA consortium.
This publication makes use of data products from the Wide-field Infrared Survey Explorer, which is a joint project of the University of California, Los Angeles, and the Jet Propulsion Laboratory/California Institute of Technology, funded by the National Aeronautics and Space Administration.
This work has made use of data from the European Space Agency (ESA) mission *Gaia* (`https://www.cosmos.esa.int/gaia`), processed by the *G*aia Data Processing and Analysis Consortium (DPAC, `https://www.cosmos.esa.int/web/gaia/dpac/consortium`). Funding for the DPAC has been provided by national institutions, in particular the institutions participating in the *G*aia Multilateral Agreement.

This publication makes use of data products from the Two Micron All Sky Survey, which is a joint project of the University of Massachusetts and the Infrared Processing and Analysis Center/California Institute of Technology, funded by the National Aeronautics and Space Administration and the National Science Foundation.
The national facility capability for SkyMapper has been funded through ARC LIEF grant LE130100104 from the Australian Research Council, awarded to the University of Sydney, the Australian National University, Swinburne University of Technology, the University of Queensland, the University of Western Australia, the University of Melbourne, Curtin University of Technology, Monash University and the Australian Astronomical Observatory. SkyMapper is owned and operated by The Australian National University's Research School of Astronomy and Astrophysics. The survey data were processed and provided by the SkyMapper Team at ANU. The SkyMapper node of the All-Sky Virtual Observatory (ASVO) is hosted at the National Computational Infrastructure (NCI). Development and support the SkyMapper node of the ASVO has been funded in part by Astronomy Australia Limited (AAL) and the Australian Government through the Commonwealth's Education Investment Fund (EIF) and National Collaborative Research Infrastructure Strategy (NCRIS), particularly the National eResearch Collaboration Tools and Resources (NeCTAR) and the Australian National Data Service Projects (ANDS).

Appendix

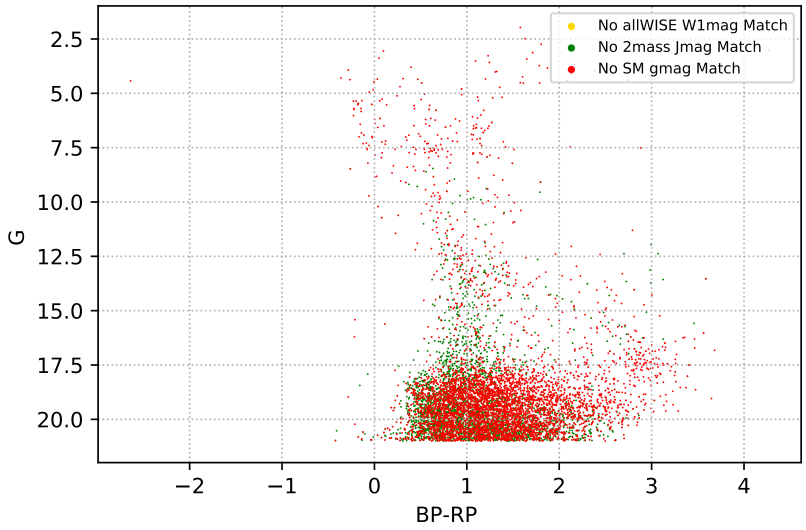

Fig. 4.1: Missing counterparts to eROSITA X-ray sources in the optical Gaia catalogue.

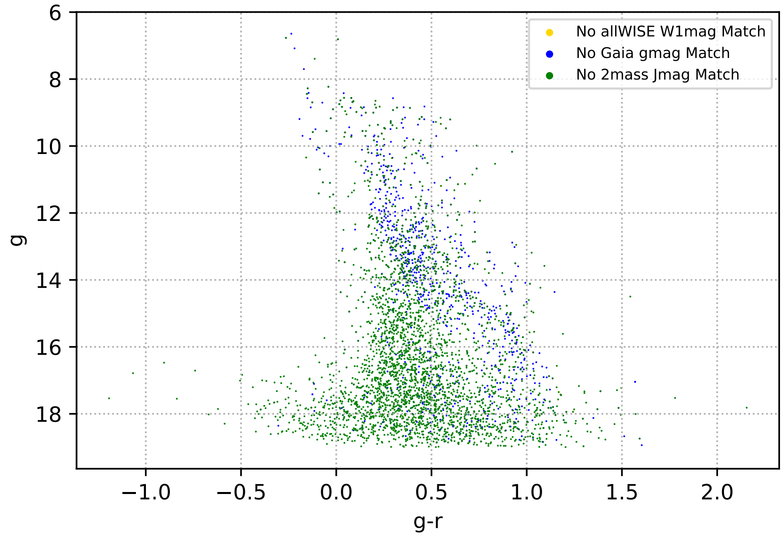

Fig. 4.2: Missing counterparts to eROSITA X-ray sources in the optical Skymapper catalogue.

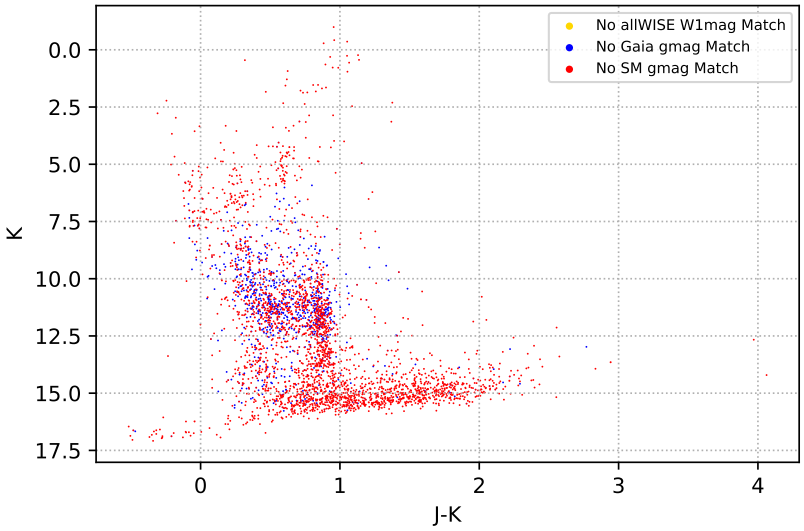

Fig. 4.3: Missing counterparts to eROSITA X-ray sources in the near-infrared 2MASS catalogue.

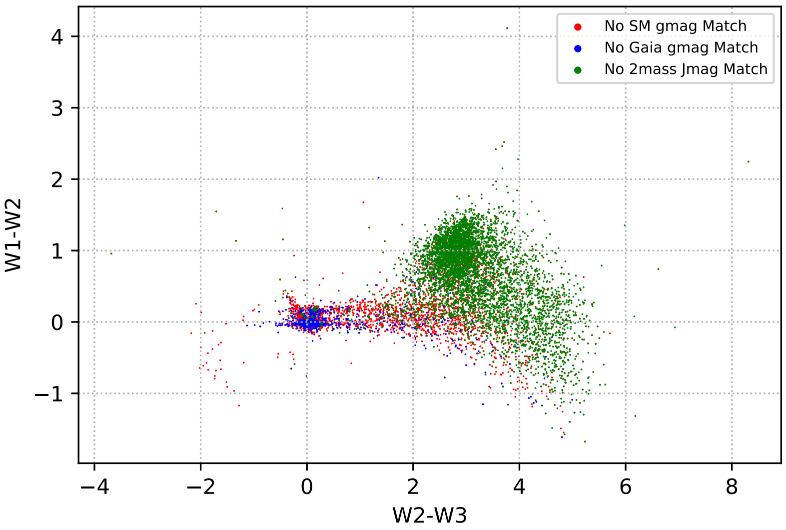

Fig. 4.4: Missing counterparts to eROSITA X-ray sources in the infrared WISE catalogue.

Eigenständigkeitserklärung

Hiermit erkläre ich, dass ich die vorliegende Arbeit selbstständig verfasst und dabei keine anderen als die angegebenen Quellen und Hilfsmittel verwendet habe.

....	....
Ort, Datum	Theresa Heindl